RSC Advances

ROYAL SOCIETY OF CHEMISTRY

PAPER

View Article Online
View Journal | View Issue

Cite this: *RSC Adv.*, 2023, **13**, 25529

ZnO-decorated green-synthesized multi-doped carbon dots from *Chlorella pyrenoidosa* for sustainable photocatalytic carbamazepine degradation†

Agnieszka Fiszka Borzyszkowska, *[ab] Agnieszka Sulowska,[a] Paweł Czaja,[c] Aleksandra Bielicka-Giełdoń, [d] Ivar Zekker[e] and Anna Zielińska-Jurek [ab]

The promising green synthesis of carbon dots (CDs) from microalga *Chlorella pyrenoidosa* was achieved using simple hydrothermal and microwave-assisted methods. Doping of nanomaterials by nonmetals (N, S, and P) was confirmed by X-ray photoelectron spectroscopy (XPS), while the existence of metals in the CDs was confirmed by inductively coupled plasma optical emission spectroscopy (ICP-OES) and transmission electron microscopy (TEM), and Mg, Ca, K, and Na were found as the dominant doped metals. The novel nanomaterials with excellent photoluminescence (PL) properties were used for the modification of ZnO obtained by a simple hydrothermal process. In this regard, a series of ZnO decorated with multi-doped carbon dots (*x*CDs) was prepared and their photocatalytic properties were evaluated. The ZnO-*x*CD photocatalysts were characterized by various advanced techniques including X-ray diffraction (XRD), Fourier transform infrared (FTIR) spectroscopy, scanning electron microscopy (SEM), XPS, Brunauer–Emmett–Teller (BET), PL, ultraviolet-visible (UV-vis) spectroscopy and electrochemical impedance spectroscopy (EIS) analysis. The photocatalytic behaviour of the obtained materials was investigated in the degradation of carbamazepine (CBZ). The influence of the synthesis method of *x*CDs and their content on the activity of the photocatalyst was examined. The photocatalyst ZnO modified with 3% *x*CDs obtained by the microwave-assisted method revealed the highest effectiveness for CBZ degradation and allowed for a first-order degradation rate of 2.85 times in comparison with non-modified ZnO. The improvement of the photocatalytic process was achieved by support with peroxymonosulphate resulting in up to 3.18 times a first order kinetic rate constant compared with that of simple photocatalysis in the presence of ZnO-*x*CDs. Taken together, our synthesized multi-doped CDs and their nanohybrids with ZnO, can be considered as promising candidates for photocatalytic applications.

Received 22nd June 2023
Accepted 19th August 2023

DOI: 10.1039/d3ra04188c

rsc.li/rsc-advances

1. Introduction

In recent years, rapid global development has caused serious environmental pollution worldwide, mostly due to persistent organic pollutants. Some organic pollutants seriously influence the living environment because they are toxic, carcinogenic, and mutagenic, and their removal by biological processes in wastewater treatment plants is inefficient. Among the variety of micropollutants, pharmaceuticals despite their low concentrations, in long-term pollution, may cause changes in the biochemical functions of aquatic organisms and related ecosystems.[1] Recent studies have indicated that carbamazepine (CBZ), an antiepileptic drug, is one of the most detected pharmaceutical compounds in water bodies[2,3] and its presence has been confirmed in freshwater and marine water, with concentrations ranging from ng dm^{-3} to a few μg dm^{-3}.[4] CBZ exhibits stability and high persistence, and its negative impacts on aquatic organisms have been proven. Recent studies on the biological effects of CBZ indicated that this compound causes altered biological responses (physiological, cellular, and molecular) at concentrations detected in the aquatic environment (up to 1 μg dm^{-3}) in marine bivalves (adults and early life stages).[5] With regard to the harmful effects of persistent organic pollutants on human beings and wildlife, the development of

---

[a] *Department of Processing Engineering and Chemical Technology, Gdansk University of Technology, Gdańsk, Gabriela Narutowicza 11/12, 80-233 Gdansk, Poland. E-mail: agnieszka.borzyszkowska@pg.edu.pl*

[b] *EcoTech Center, Gdańsk University of Technology, G. Narutowicza 11/12, 80-233 Gdansk, Poland*

[c] *Institute of Metallurgy and Materials Science, Polish Academy of Sciences, Reymonta 25 St, Krakow, Poland*

[d] *Faculty of Chemistry, University of Gdansk, Stwosza 63, 80-308 Gdansk, Poland*

[e] *Institute of Chemistry, University of Tartu, 14a Ravila St., 50411 Tartu, Estonia. E-mail: ivar.zekker@ut.ee*

† Electronic supplementary information (ESI) available. See DOI: https://doi.org/10.1039/d3ra04188c

advanced treatment technologies is crucial to face this challenge. Among the various water treatment techniques employed to remove micropollutants from water streams, for example adsorption, membrane separation, coagulation, and advanced oxidation processes (AOPs) are promising for the elimination of organic micropollutants, especially for recalcitrant compounds with a low biodegradability.[6,7] In this regard, solar light-assisted photocatalytic degradation of recalcitrant pollutants in the presence of an advanced semiconductor offers efficient water treatment solution from pharmaceutical drugs.[8]

Zinc oxide (ZnO) is a promising photocatalyst owing to its nontoxicity, simplicity of processing and synthesis, excellent photostability, high chemical stability, and low cost.[5,9] These advantages make ZnO applications in photocatalytic technologies highly widespread in industrial applications. However, certain limitations to common applications, such as the narrow photoresponse range, recombination of photogenerated electron–hole pairs, and low adsorption capacity, have guided extensive studies on appropriate modifications to enhance the photoreactivity of ZnO.[10] Therefore, much effort has been devoted to improve the photocatalytic activity of ZnO using *e.g.*, doping with various metals[11,12] and non-metals,[13] formation of hetero-structural composites,[14] noble metals deposition,[15] and coupling with nanocarbon components.[10,16]

Zero-dimensional quasi-spherical nanoparticle carbon dots (CDs) have gained global importance in many applications. CDs, in particular, exhibit excellent advantages including facile synthesis, good luminescence features, photostability, low cytotoxicity, low risk to the environment, and easy functionalization for surface modification.[17] Among the variety of reported CD synthesis methods, *e.g.*, carbonization method,[18] pyrolysis,[19] hydrothermal,[20,21] microwave irradiation,[22,23] arc discharge,[24] electrochemical exfoliation,[25] laser ablation,[26] and acidic oxidation.[27] Methods considered as a green bottom-up synthesis approach are hydrothermal carbonization and microwave irradiation.[28] Green CDs syntheses methods are promising because of its facile process, the use of an aqueous medium, and the possibility of using carbon from diverse renewable organic resources.[28,29] Among the aforementioned methods, the microwave-assisted method allows for the synthesis of shorter reaction times and lower reaction temperatures and does not require a specialized Teflon reactor.[30]

Following the trend of green chemistry principles, the development of biomass-derived CDs is of great interest. Various bio-waste/plant materials,[29] including plants,[31] mushrooms,[32] and microorganisms[33] offer cost-effective and eco-friendly precursors for the synthesis of CDs. In particular, algae with alkaloids, proteins, polyketides, quinones, cyclic peptides, phlorotannins, polysaccharides, lipids, and glycerol can be used to synthesize CDs nanoparticles with a high number of heteroatoms (N, S and P) on the surface, which is required for achieving a high quantum yield.[34] Zhang *et al.* synthesized N-, S-, and P-doped CDs from microalgae *Chlorella pyrenoidosa* with main model ingredients (*i.e.*, glucose, glycine, and octadecanoic acid).[33] Hydrothermal-produced N-, S-, P-doped CDs with a diameter smaller than 20 nm revealed fluorescence quantum yield 4.7–9.4 times higher than CDs produced from model compounds.[33]

Owing to their numerous advantages, CDs have been used to improve the effectiveness of semiconductors for the use in photocatalytic processes. These directions provide useful strategies for the treatment of pharmaceuticals, pesticides, and other industrial pollutants in water. CDs offer a variety of benefits: (i) light absorption in the visible region by combination with semiconductors in their hybrids, (ii) upconversion photoluminescence, (iii) CDs act as electron acceptors to reduce the recombination of photogenerated electron–hole pairs, and (iv) photosensitization of photocatalysts.[35,36] A series of recent studies have indicated that the utilization of CD for inorganic semiconductors modification may enhance photocatalytic activity. For instance, Silva *et al.*[37] demonstrated that TiO_2/carbon quantum dot composites possessed improved photodegradation efficiency of antibiotics, such as sulfadiazine, sulfamethoxazole and trimethoprim under UV-vis irradiation. Also, Ren and coworkers[38] have provided evidence for the boosting tetracycline photodegradation under visible light using carbon quantum dots/Bi_2WO_6 heterojunctions as the photocatalysts. In general, carbon dots influence positively on organic compounds degradation by the photocatalytic treatment.

Many studies have confirmed that the oxidizing capability of a photocatalyst can be significantly improved by the assistance of *e.g.*, hydrogen peroxide (H_2O_2), peroxymonosulphate (PMS) or persulphate (PS).[14,39,40] This enhancement is caused by the activation of these oxidants by photoinduced electrons to generate radicals with a strong oxidation potential, such as hydroxyl ($^{\bullet}OH$) with a redox potential of 2.8 V or sulphate radicals ($SO_4^{\bullet-}$) with even a higher redox potential (2.5–3.1 V) depending on their activation methods.[39] Additionally, $SO_4^{\bullet-}$ possesses a higher selectivity and longer half-life than $^{\bullet}OH$ in certain cases. Thus, $SO_4^{\bullet-}$ is expected to have better capacity for organic pollutants degradation.[41,42]

In this study, we report environmentally-friendly microwave-assisted and hydrothermal methods to prepare multi-doped CDs from freshwater algae *Chlorella pyrenoidosa*. Furthermore, both types of multi-doped CDs were applied to produce novel multi-doped CDs-ZnO nanoparticles (NPs) by simple hydrothermal method, which exhibited enhanced photocatalytic performance to remove CBZ under a Xenon lamp. The multi-doped CDs-ZnO also were examined in the photocatalytic process assisted by peroxymonosulphate (PMS). The phase, morphologies, optical and electronic properties of the synthesized materials were investigated in detail. The mechanism of the photocatalytic process supported by PMS was examined by the experiments in the presence of scavengers. Reusability studies were also carried out using selected nanocomposites to recognize the long-term stability and commercial applications.

2. Materials and methods

2.1. Materials

Microalgae tablets were purchased from Meridian, Taiwan. The freshwater algae *Chlorella pyrenoidosa* was in the form of

200 mg tablets, prepared using the patented DynoMill® method, causing the cell walls to break (Broken Wall).

Zinc acetate dihydrate ($(CH_3COO)_2Zn \cdot 2H_2O$, an analytical reagent grade) was purchased from AppliChem (Germany). Sodium hydroxide (NaOH, 99.9%) and 2-propanol ($(CH_3)_2CHOH$, 99.9%) were obtained from POCh (Poland). Carbamazepine ($C_{15}H_{12}N_2O$, 99.9%), potassium peroxymonosulphate (PMS, $2KHSO_5$ $KHSO_4$ K_2SO_4, OXONE®), *p*-benzoquinone (98%), *tert*-butanol (>99.5%), ammonium oxalate monohydrate ($(NH_4)_2C_2O_4$, 99.5%), and sodium azide (NaN_3, 99.5%) were obtained from Sigma-Aldrich. Acetonitrile (ACN, CH_3CN, LCMS grade) was obtained from Supelco, and orthophosphoric acid (H_3PO_4, HPLC electrochemical grade reagent) was purchased from Fisher Chemical (USA). The chemical reagents were used as obtained without additional purification. Deionized water (DI) produced by Hydrolab equipment, was used in all experiments.

2.2. Multi-doped carbon dots preparation

2.2.1. Hydrothermal method. Firstly, 2.5 g microalgae powder was obtained by grinding in a mortar and then dispersing in 150 cm^3 of deionized water using an ultrasound bath for 15 min. The microalgae powder dispersion was transferred to a Teflon-lined stainless steel autoclave and heated at 200 °C for 4 h in an oven. Afterward, the reaction mixture was cooled to room temperature, and the sediment was removed by centrifugation (6000 rpm, 10 min) and thereafter solution was filtered. Next, the supernatant containing the CDs was transferred to an amber-coloured storage bottle and labelled as hydrothermal-assisted CD (CD_ht). The CD_ht solution was freeze-dried for further characterization.

2.2.2. Microwave-assisted method. Firstly, 2.5 g microalgae powder was obtained by grinding in a mortar and then dispersing into 10 cm^3 of deionized water, followed by stirring for 15 min. The microalgae powder dispersion was then treated by microwave irradiation at 750 W for 7 min. The solid powder was ground in a mortar and dispersed in 150 cm^3 of deionized water by ultrasonication for 15 min. Next, the solids were removed by centrifugation (6000 rpm, 10 min) and solution was filtered through a 0.22 μm filter membrane. Subsequently, the supernatant containing the CDs was transferred to an amber-colored storage bottle and labelled as microwave-assisted CD (CD_mw). For further characterization, solution of CD_ht was freeze-dried.

2.3. Preparation of ZnO-multi-doped CD nanocomposites

ZnO-*x*CD photocatalysts were prepared *via* a hydrothermal process under mild conditions. For the synthesis, firstly, ($(CH_3COO)_2Zn \cdot 2H_2O$, 20 mmol)) was dissolved in deionized water (50 cm^3) under constant magnetic stirring. Secondly, appreciable volumes of the previously prepared CD aqueous solutions (0, 5, 10, and 20 cm^3 of CD_mw, which were linked to 0, 0.75, 1.5, and 3 wt% and 0.612, 1.25; 2.5 cm^3 of CD_ht, which were linked to 0.75, 1.5, and 3 wt%) were added. Appreciable amounts of CD_mw and CD_ht were added according to the mass obtained after lyophilization. After homogeneous dispersion, 50 cm^3 of NaOH aqueous solution (60 mM, 2.4 g) was added to the solution of Zn salt and CD and stirred at room temperature for 5 min. The suspension was then placed in a Teflon-lined stainless-steel autoclave and heated at 80 °C for 16 h in an oven. Finally, the photocatalysts were washed with deionized water until neutral pH was obtained and dried at 50 °C for 12 h.

2.4. Characterization

X-ray diffraction (XRD) analysis were carried out by using X-ray diffraction (XRD) system SmartLab (Rigaku Intelligent, Tokyo, Japan). XRD patterns were recorded at 2θ from 5° to 80°, with a scan speed of 2° min^{-1} and a step of 0.01°. Specific surface area was evaluated by nitrogen adsorption with the Brunauer–Emmett–Teller (S_{BET}) method with the Micromeritics Gemini V apparatus (model 2365) (Norcross, GA, USA). The optical properties of the samples were analysed by the ultraviolet-visible diffuse reflectance spectra (DRS) in the wavelength range from 200 nm to 800 nm by the Thermo Scientific Evolution 220 diffuse reflectance spectrophotometer (Waltham, MA, USA) using barium sulphate as a standard reference for powder samples and using water as a standard for liquid samples. Photoluminescence (PL) studies were performed on a RF-6000 spectrofluorometer (Shimadzu, Japan). A PerkinElmer ICP-OES Optima 2000 DV (USA) was used to determine metals (Al, As, Bi, Ca, Cd, Cr, Co, Cu, Fe, Ga, In, K, Mg, Mn, Na, Ni, Pb and Zn) in the studied samples. The ICP-OES instrument was optimized before measurement and was used with the following parameters: RF power, 1300 W; frequency 40 MHz, demountable quartz torch, axial viewing, plasma gas (Ar) flow, 15.0 dm^3 min^{-1}; auxiliary gas (Ar) flow, 0.2 dm^3 min^{-1}; nebuliser gas (Ar) flow, 0.8 dm^3 min^{-1}; glass cyclonic spray chamber, sample pump flow rate, 1.5 cm^3 min^{-1}; replicate, 3. Metals ions were measured at wavelengths of 396.153; 193.696; 223.061; 317.933; 228.802; 267.716; 228.616; 327.393; 238.204; 417.206; 230.606; 766.490; 285.213; 257.610; 589.592; 231.604; 220.353; 206, and 200 nm for Al, As, Bi, Ca, Cd, Cr, Co, Cu, Fe, Ga, In, K, Mg, Mn, Na, Ni, Pb, and Zn, respectively. The total amount of metals in the studied microalgae was determined after the digestion process using nitric acid. Fourier transform infrared (FTIR) spectra were recorded on a FTIR Nicolet iS10 (Thermo Fisher Scientific Waltham, MA, USA) spectrometer in the wavenumber from 400 to 4000 cm^{-1}. The pellets were made by grounding the sample and KBr in 1 : 100 ratio and pressed using a hydraulic press. The surface chemistry of the samples was analysed by X-ray photoelectron spectroscopy (XPS) using the UHV Prevac spectrometer with monochromatic Al Kα radiation (hn = 1486.6 eV) from an X-ray source operating at 10 kV. The Casa XPS Version 2.3.23 PR1 software was used to analyse the XPS data. Transmission electron microscopy (TEM) investigations were conducted with ThermoScientific Titan Themis Cs corrected 200 kV S(T)EM. Samples were dispersed in ethanol and subsequently placed on a carbon-coated copper grid. The morphology of samples was analysed using Phenom ParticleX Desktop SEM form Thermo Fisher Scientific (USA), which was equipped with backscattered electrons (BSEs) and secondary electrons (SEs) detector. Thermogravimetric analysis (TGA) was performed using thermogravimetric analyser 2 SF/1100 from Mettler Toledo. The thermal properties of samples with the mass of 7–10 mg were investigated at the temperature range of 50 °C to 800 °C (heating rate 10 °C min^{-1}), under nitrogen atmosphere (N_2 flow rate 50 cm^3 min^{-1}). Electrochemical characterization of the prepared samples was performed by electrochemical impedance spectroscopy (EIS), photocurrent measurements, and Mott–Schottky measurements using an Autolab PGSTAT204 potentiostat/galvanostat equipped with an FRA32M module and an on–off light-emitting diode (LEDs) of near-ultraviolet (390 nm) as the illumination source. The photocatalysts were deposited on screen-printed carbon electrodes (DRP-110 type) from an aqueous suspension. Typically, 10 mg of the photocatalyst was dispersed in 2 cm^3 of water, mixed, and ultrasonicated, and the working electrode was coated with 0.01 cm^3 of suspension and finally dried at 60 °C. The electrolyte used was Na_2SO_4 with a concentration of 1 M. EIS was performed under dark and light conditions with frequencies in the range of 105–0.1 Hz and a sinusoidal wave of 5 mV. The transient photocurrent was measured at a constant potential of 0 V. During the experiment, the deposited electrode was irradiated in the following sequence: light-off (50 s) and light-on (50 s).

2.5. Photocatalytic performance measurements

The photocatalytic activities of the ZnO-*x*CD were evaluated in the degradation of carbamazepine (CBZ) under UV-vis light. The photodegradation processes were performed in a quartz reactor with aeration, constant temperature of 20 °C, and sampling system. The photocatalyst at the content of 0.5 g dm^{-3} and 25 cm^3 of the CBZ aqueous solution (14 mg dm^{-3}) was introduced into the reactor and kept in the dark for 30 min under magnetic stirring to reach adsorption–desorption equilibrium. The light intensity was measured using a UV radiometer (UV-B) and was maintained at approximately 25 mW cm^{-2}. At certain time intervals, 1 cm^3 of the suspension solution was filtered through syringe filters (φ = 0.2 μm) to determine the CBZ concentration and total organic carbon (TOC) after each process. Moreover, some processes were supported by adding 0.2–2 mM PMS to the suspension at the beginning of irradiation. The reaction solution containing PMS was immediately quenched by the addition of methanol. The presence of CBZ was monitored using a high High-Performance Liquid Chromatography with Diode-Array Detection system (HPLC-DAD, Kyoto, Japan) equipped with a Phenomenex Kinetex C-18 column. The mobile phase, consisting of ultrapure water (A), acetonitrile (B), and H_3PO_4 was eluted in the isocratic mode, in a ratio of 72% (A)/27.5% (B)/0.5% (C), with a flow rate of 1.5 cm^3 min^{-1}. The temperature of the chromatographic column was maintained at 40 °C, injection volume was 0.01 cm^3, and detection wavelength was 285 nm. TOC was measured using a carbon analyser (TOC-L, Shimadzu, Kyoto, Japan).

Stability tests were performed using the most active photocatalysts supported by the PMS-assisted process. Detailed experiments on the effect of ions were performed at a concentration of 10 mM NaCl, $NaHCO_3$, and $NaNO_3$ (to assess the effect of Cl^-, HCO_3^-, and NO_3^-, respectively), while the pH was adjusted with NaOH (0.1 M) and HNO_3 (0.1 M). Moreover, the contributions of selected reactive species generated during photocatalysis were examined. The contributions of $^{\bullet}OH$ and $SO_4^{\bullet-}$, $^{\bullet}OH$, h^+, $O_2^{\bullet-}$, and $^1O_2$ were determined by conducting the degradation processes of CBZ in the presence of isopropanol (IPA) (5 mM), *tert*-butanol (TBA) (5 mM), ammonium oxalate (AO) (5 mM), benzoquinone (BQ) (1 mM), and sodium azide (SA) (5 mM), respectively.

3. Results

3.1. Characterization of multi-doped carbon dots

In this study, carbon dots (CD) were prepared using two separate methods: hydrothermal (CD_ht) and microwave-assisted (CD_mw). In both cases, *Chlorella pyrenoidosa* was used as the raw material for CD. The schematic preparation methods for CD are depicted in Fig. 1. First, microscopic analysis was performed to determine the CD size and chemical composition. Based on the STEM image presented in Fig. 2a, the CDs were predominantly monodispersed and spherical. The particle size distribution in Fig. 2b reveals that CD_ht ranged from 12 to 70 nm, with an average size of 23 nm. The SEM high-angle annular dark field (STEM-HAADF) image and corresponding elemental mapping images of CD_ht (Fig. 2c) demonstrate the presence and coexistence of carbon (C), oxygen (O), phosphorus (P), sulphur (S), calcium (Ca), and magnesium (Mg) elements. Carbon was spread over the picture owing to the use of carbon-coated grids during the analysis.

In the case of CD_mw, microscopic analysis confirmed the spherical shape of the particles (Fig. 3a). However, the particle size distribution in Fig. 3b was much larger than that of CD_ht. The size of CD_mw ranged from 21 to 192 nm, and the mean size was approximately 68 nm. Elemental color mapping, shown in Fig. 3c, confirmed the presence of C, O, P, S, Ca, and Mg in CD_mw. In summary, the preparation method of CDs from microalgae strongly influenced the size of the CDs. Further analysis was performed to determine differences in the

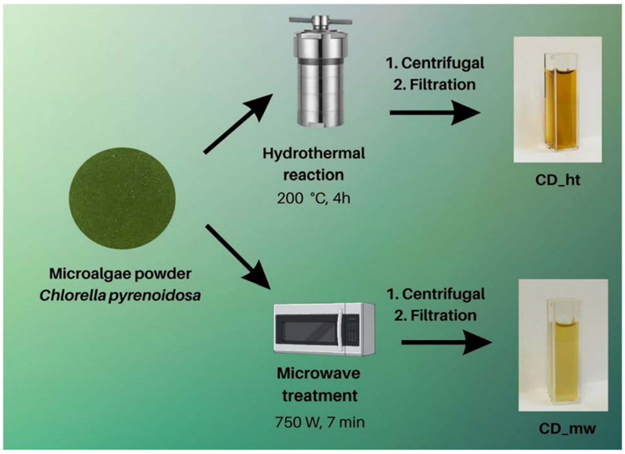

Fig. 1 Preparation methods of CDs derived from the algae *Chlorella pyrenoidosa* by hydrothermal and microwave treatment.

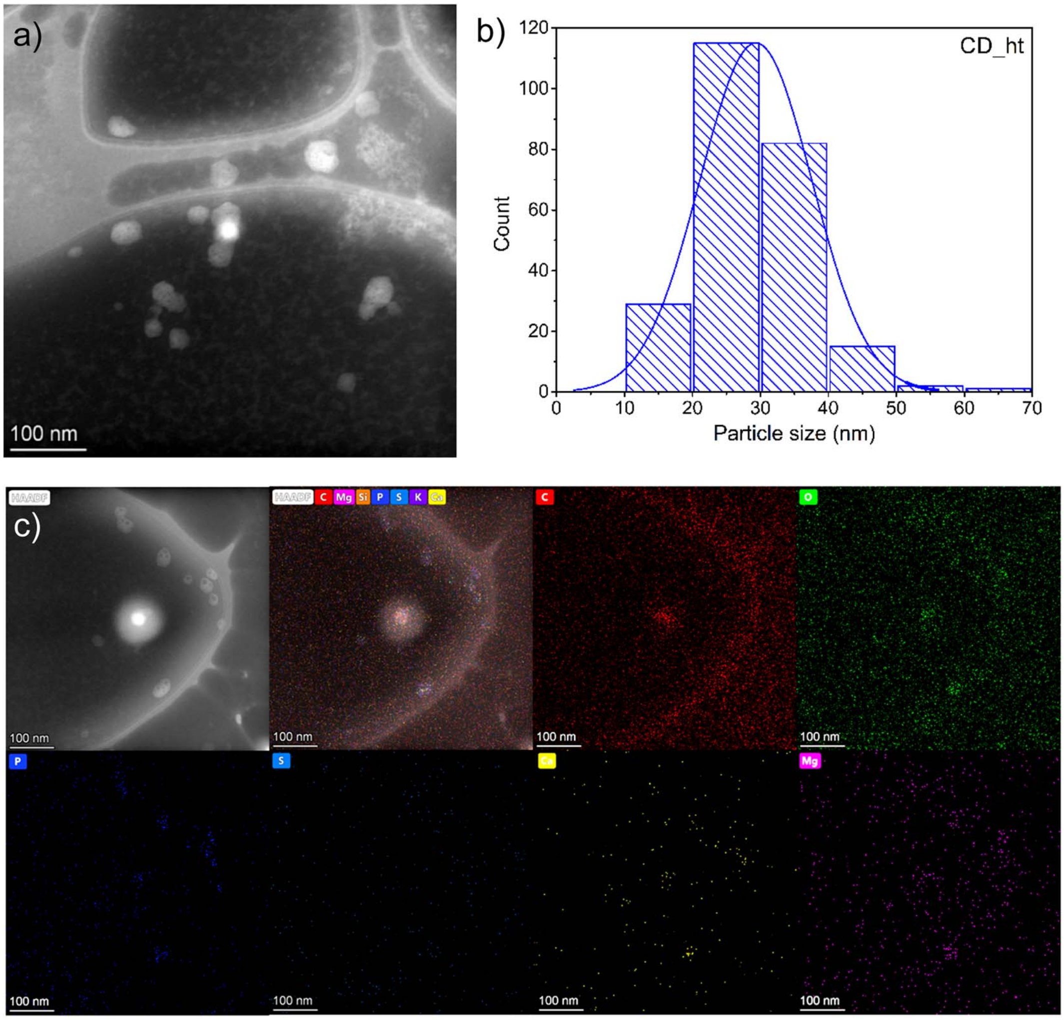

Fig. 2 (a) STEM image, (b) particle-size distribution (c) elemental (C, O, P, S, Ca and Mg) mapping images of CD_ht.

chemical structures and optical properties of the obtained CDs samples.

ICP examination was used to determine the metal concentration in the M-doped CDs nanoparticles synthetized by hydrothermal and microwave-assisted method, as well as the metal content in the microalgal tablets, which were the source for the synthesis of CD. The solutions of CDs and were analysed for selected metals (Al, As, Bi, Ca, Cd, Cr, Co, Cu, Fe, Ga, In, K, Mg, Mn, Na, Ni, Pb, and Zn) and the results (Table 1) show different doping levels depending on the metal. The highest concentration of metals in CDs samples were found for Ca, Mg, Na and K for CD_ht, as well as for CD_mw. According to the measurement of metal content in microalgae tablets, these metals were also at the highest level in the source material. Up to that we can observe that analysed heavy metals are under detection level or very low concentration up to 0.006 mg dm^{-3} for Cr CD_ht. Therefore, we can assume that produced CDs are environmentally-friendly and the concentration of metals is associated with metals incorporated into CDs as is shown on the TEM images, where we can observe clusters of metals related with CDs. According to these results we have proven that the synthesized CDs are multi-metal doped particles, with the main contribution of Ca, Mg, Na, and K.

FTIR analysis was used to determine the chemical functional groups of the obtained carbon dots, and the results are shown in Fig. 4. Generally, the spectra of the CDs had similar peaks, and all the CDs showed broad stretching vibrations at 3000–3550 cm^{-1}, which were assigned to the surface hydroxyl group and N–H of primary amines.[43] The peaks centred at approximately 2930 cm^{-1} and 2960 cm^{-1} originate from the C–H stretching modes of the alkyl chains. In both CDs samples, the absorption band for the C=O stretching mode connected to the N–H deformation mode was registered at 1664–1671 cm^{-1}, which confirmed the presence of primary amide functional groups.[44,45] The peak detected at 1454 cm^{-1}, which was registered in both spectra, characterized the C–H bending vibration of the methyl group. The bands at 1610 cm^{-1} and 1592 cm^{-1} for CD_mw and CD_ht, respectively, were attributed to the C=C stretching vibration.[44] In addition, the C–O stretching vibrations of the hydroxyl groups were registered in the range of 1087–1078 cm^{-1} for both CD materials.[46] The medium peak at 1234 cm^{-1}, assigned to C–N stretching in amine, was recorded

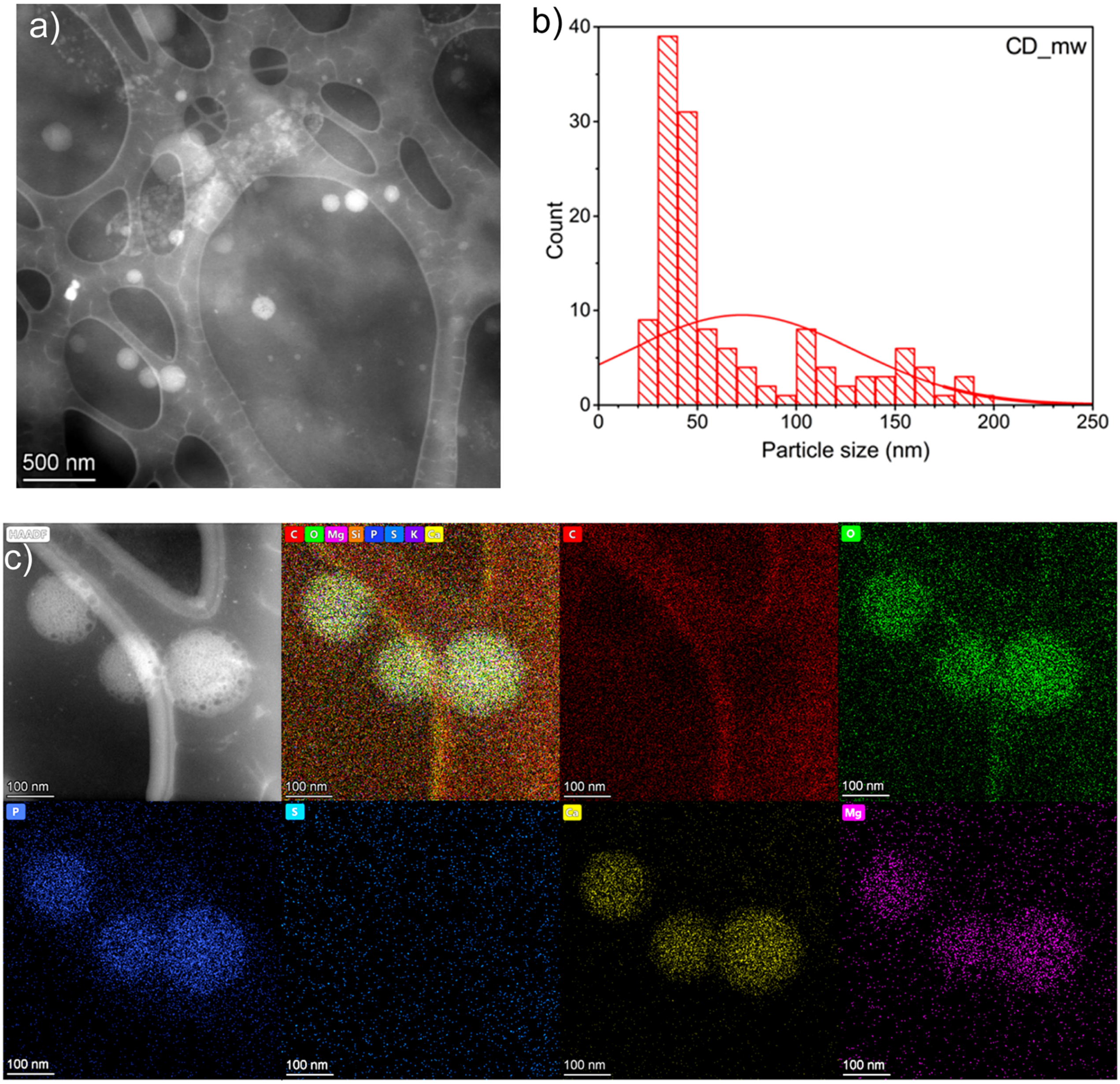

Fig. 3 (a) STEM image, (b) particle-size distribution, and (c) elemental (C, O, P, S, Ca and Mg) mapping images of CD_mw.

only for CD_mw.[44] The microthermal synthesis conditions were milder in terms of temperature and pressure, comparing with hydrothermal synthesis. According to the available literature studies, amino acids decompose thermally, causing formation of inorganic gases,[47] therefore C–N stretching vibration is not observed for CD_ht. The vibrations of CO_2 at 2360 cm^{-1} and 2342 cm^{-1} were observed in both CDs spectra. Peaks indicating the presence of C–S or C–P bonds in the obtained CDs were not detected.

XPS was performed to investigate the surface composition and oxidation states of the elements in the CD_ht and CD_mw samples. The XPS survey spectra of CD_ht and CD_mw are shown in ESI in Fig. S1.† The high-resolution C, O, N, S, and P spectra of analysed samples are shown in Fig. 5. The C 1s spectra were analysed based on model of Koinuma *et al.*,[48] which was enriched with splitting the carboxyl group peak into two, as in Radaelli's work,[49] and with a peak corresponding to carbon bound to nitrogen (C–N).[50,51] The C 1s spectrum of both carbon materials was fitted into nine peaks at 284.6, 285.0, 285.5, 285.9, 286.4, 287.0, 288.1, 288.9, and 289.6 eV, corresponding to C=C, C–H, C–C, C–N, C–OH, C–O–C, O=C–OH, and CO_3^{2-}, respectively. However, the percentage atomic concentration of identified carbon bonds differed between CD_ht and CD_mw samples. For example, CD_mw possessed 26.7% C–H bonds, and CD_ht had 17.2% analogous bonds on the surface. In addition, CD_mw was characterized by a greater number of C–C bonds, which was 22.8% in comparison to CD_ht (17.5%). In contrast, the atomic concentrations of C–OH

Table 1 Summary table of the ICP data for CD_ht, CD_mw and microalgae tablets

	Metal concentration (mg dm^{-3})		Metal content (μg g^{-1})
Analyte name	CD_ht	CD_mw	Microalgae tablets
Cu 327.393	0.0040 ± 0.000	0.0010 ± 0.0001	0.816 ± 0.027
Cr 267.716	0.006 ± 0.0001	0.001 ± 0.0000	0.7010 ± 0.011
Cd 228.802	<0.001	<0.001	<0.0866
Ni 231.604	<0.001	<0.001	1.299 ± 0.036
Pb 220.353	<0.001	<0.001	<0.0866
Zn 206.200	2.013 ± 0.006	0.004 ± 0.0002	9.03 ± 0.14
Fe 238.204	0.064 ± 0.001	0.262 ± 0.0022	307.2 ± 1.2
Mn 257.610	0.446 ± 0.002	0.0770 ± 0.0004	45.46 ± 0.57
Ca 317.933	16.410 ± 0.074	7.98 ± 0.13	1262 ± 21
Mg 285.213	43.30 ± 0.24	8.507 ± 0.001	2750 ± 16
Na 589.592	15.28 ± 0.12	10.46 ± 0.12	1116.0 ± 5.0
K 766.490	62.56 ± 0.072	30.14 ± 0.065	4774 ± 54
Al 396.153	0.551 ± 0.0004	0.040 ± 0.0004	30.00 ± 0.44
Co 228.616	0.003 ± 0.0000	0.003 ± 0.0001	1.761 ± 0.009
As 193.696	<0.002	<0.002	<0.173
Bi 223.061	<0.001	<0.001	<0.0866
Ga 417.206	<0.0015	<0.0015	0.613 ± 0.009
In 230.606	<0.001	<0.001	<0.0866

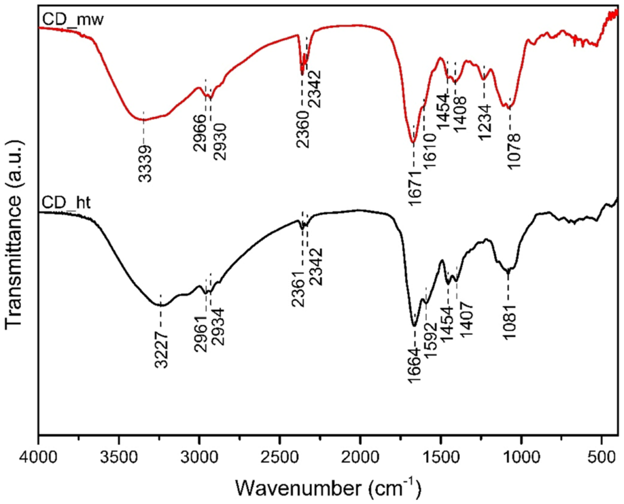

Fig. 4 FTIR spectra of CD_ht and CD_mw.

were 21.4% and 15.2% for CD_ht and CD_mw, respectively. The signals identified as carbon from carboxyl groups were considerably higher for CD_ht than for CD_mw. XPS analysis revealed the presence of similar amounts of nitrogen-bonded carbon, which was 6.8% for CD_ht and 5.2% for CD_mw. Four distinct signals in the O 1s region were identified in the obtained CDs, which were assigned as followed: (i) 531.0 eV for O=C in carbonyl groups, (ii) 531.8 eV for O=C–O in carboxyl groups or P=O phosphorus–oxygen double bond, (iii) 532.8 eV for C–OH in aliphatic or aromatic carboxyl groups, or C–O–C ether functional groups, and (iv) 533.9 eV for C–O–C in epoxy groups, O–C=O of carboxyl groups, or P–OH phosphorus–oxygen single bond.[52] For both CD_ht and CD_mw, the area of peaks at 532.8 eV and 533.9 eV was similar. The main differences between samples in the oxygen region were seen for peaks at 531.0 eV and 531.8 eV. The atomic concentrations of O=C carbonyl groups in CD_ht and CD_mw were 5.4% and 12.1%, respectively. In addition, the intensity of peak assigned to O=C–O or P=O was greater for CD_ht (37.8%) than for CD_mw (27.1%). The curves for N 1s of both CD materials were fitted to three distinct nitrogen: (i) 401.8 eV for O=C–N of amide, (ii) 400.3 eV for =N– in amine groups, and (iii) 399.4 eV of protonated nitrogen =NH^{+}–.[53–55] CD_ht was characterized by the following nitrogen atomic concentration: 17.1% of nitrogen originating from amide groups, 71.1% of nitrogen of amines, and 11.8% of protonated nitrogen. In comparison, CD_mw consisted of 11.7% of the nitrogen in amides, 59.3% of amines, and 29.0% of protonated nitrogen. A sulphur in form of sulphates and phosphor as phosphates were detected in both CD_ht and CD_mw materials. The atomic concentrations of S in CD_ht and CD_mw were 0.5% and 0.9%, respectively. P was present in CD_ht and CD_mw in amount 0.4 at% and 1.7 at%, respectively.

To explore the optical properties of the CDs, their absorption spectra were recorded, as shown in Fig. 6a. In both the CDs solutions, strong absorption was observed in the UV region, which was attributed to the π → π* transition of the C=C bonds. The absorption peaks at 251 nm for CD_ht and 256 nm for CD_mw originate from the *n* → π* transition of C=O and/or C–N bonds.[46] The lower absorption intensity of the *n* → π* transition of the CD_ht sample could be attributed to the lower content of the above-mentioned functional groups compared with that of the CD_mw.[56] This indicates that the preparation method influences the chemical structure of the obtained CDs. In this study, the CDs obtained by the microwave-assisted preparation method possessed higher contents of C=O and C–N bonds than those obtained by the hydrothermal method.

Fig. 6b shows the XRD patterns of the CDs, which reveal a single broad diffraction peak centred at 21.5° for CD_mw and

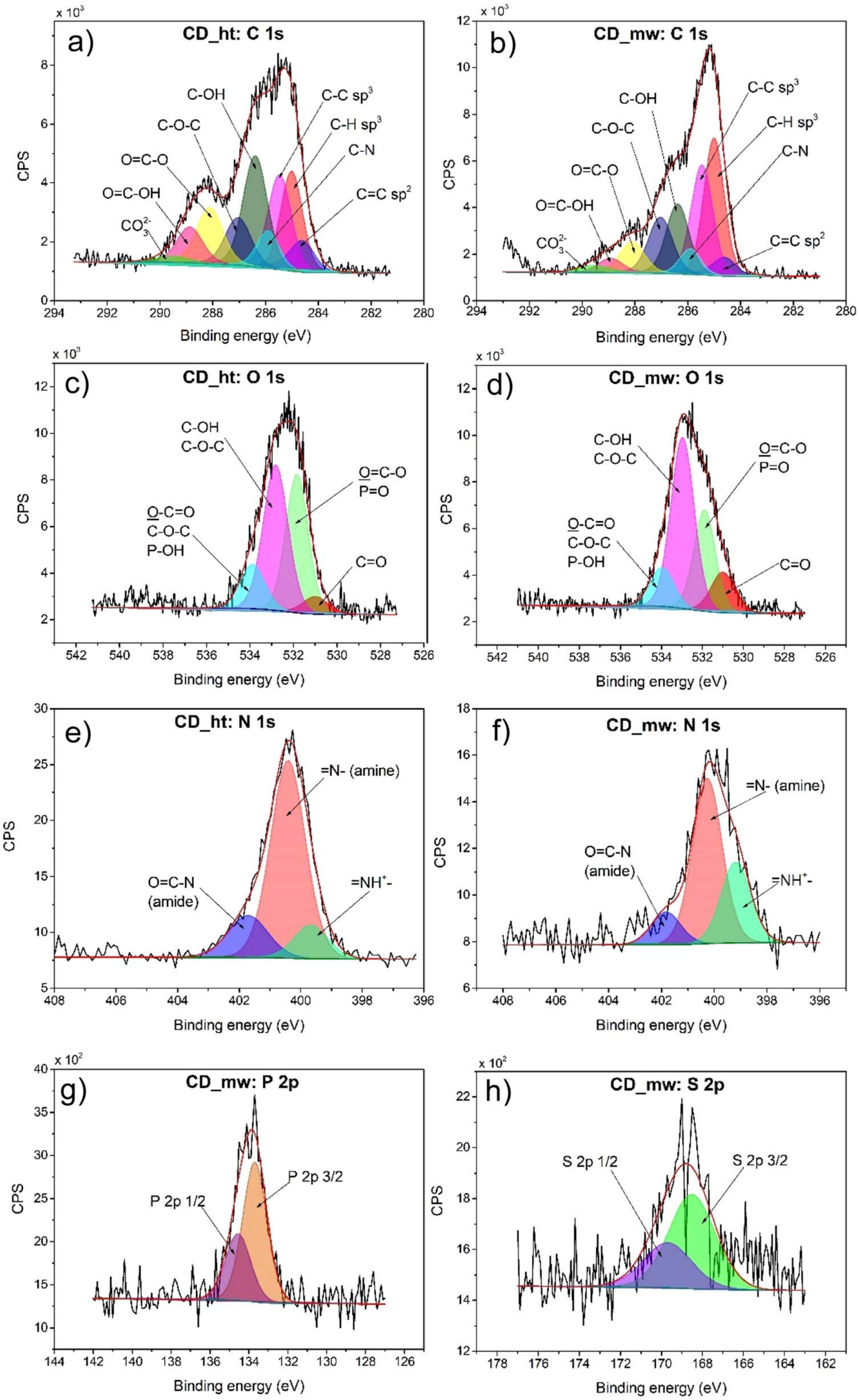

Fig. 5 High-resolution deconvoluted XPS spectra for C (a and b), O (c and d), N (e and f), P (g), and S (h) in the CD_ht and CD_mw samples.

20.5° for CD_ht indexed to the (002) plane for both samples (JCPDS CARD no. 08-0415). The interlayer distance of CDs calculated using Bragg's equation were 0.31 nm and 0.32 nm for CD_ht and CD_mw, respectively. The higher value of CD_ht can be attributed to the presence of more oxygen functional groups. Both materials were characterized by the more amorphous nature of graphite (0.13 nm).[57]

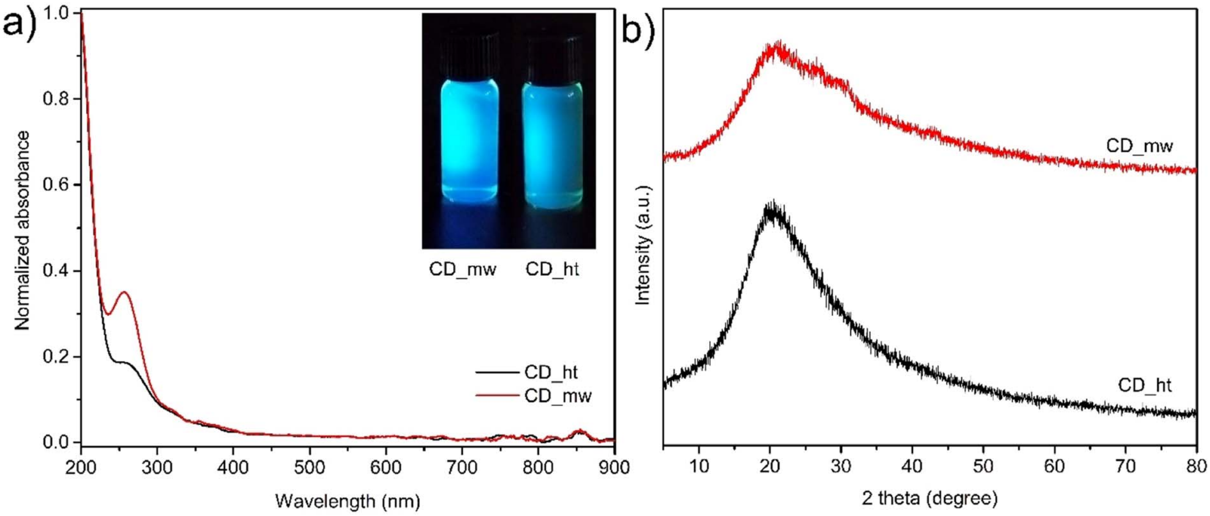

Fig. 6 (a) UV-vis absorption spectra of CD_mw and CD_ht, digital photographs of CDs solutions irradiated at 390 nm (inset), and (b) XRD patterns of CD_ht and CD_mw.

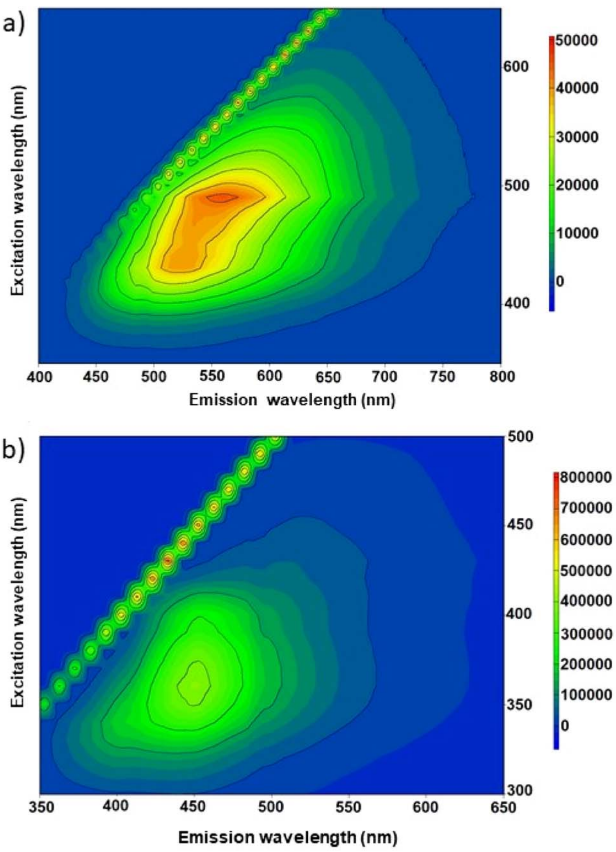

Fig. 7 2D PL spectra under excitation wavelengths range from 300 to 800 nm for (a) CD_ht and (b) CD_mw.

Fig. 7a and b show the excitation–emission contour maps of the CD_ht and CD_mw aqueous solutions, respectively. The PL spectra were recorded at room temperature under different excitation wavelengths. The CDs derived from the microalgae exhibited a characteristic excitation wavelength-dependent emission spectral nature. For CD_ht, the strongest emission appeared at 550 nm, with an excitation wavelength of 490 nm. When the excitation wavelength was varied from 400 to 550 nm, the emission peaks red-shifted from ~500 to ~600 nm, which is evident from the 2D emission–excitation map (Fig. 7a). In the case of CDs _mw, the strongest emission appeared at 450 nm, with an excitation wavelength of 360 nm. Red shifting of this sample was also observed at excitation wavelengths varying from 320 to 400 nm, revealing emission from ~430 to ~460 nm. According to previous studies, both types of CDs exhibit good fluorescence properties with existing red shifting, indicating their attribution to the quantum size effect.[58,59]

TGA was performed to study the thermal degradation profiles of CD_ht, CD_mw, and the microalgae tablets (Fig. 8). The weight loss before 120 °C was attributed to the elimination of chemisorbed water from the material. In the case of the raw material for obtaining CDs, *i.e.*, microalgae weight loss of 5.15% was recorded at 125 °C and 64.55% weight loss was observed in the range of 165–550 °C. The weight loss of CD_ht was also recorded at two main temperatures between 65 °C and 120 °C and 134–550 °C with 5.11% and 55.13% weight losses, respectively. For CD_mw, the first thermal degradation step was 2.84% and it was observed at 126 °C; the main weight loss occurring between 200 °C and 550 °C was 55.45%. The thermal stabilities of the multi-doped CDs obtained using the two different methods were approximately the same, with slight differences in the 120–500 °C range because of differences in chemical composition and doping groups. In this study, the differences in the chemical structures of CD_ht and CD_mw were confirmed by the DR/UV-vis, PL, and XPS spectra.

3.2. Characterization of ZnO-*x*CD nanocomposites

The XPS survey scan spectra of the ZnO-3CD_mw nanocomposite and the reference ZnO catalysts are shown in Fig. 9. The high-resolution XPS spectra of Zn 2p and O 1s confirmed

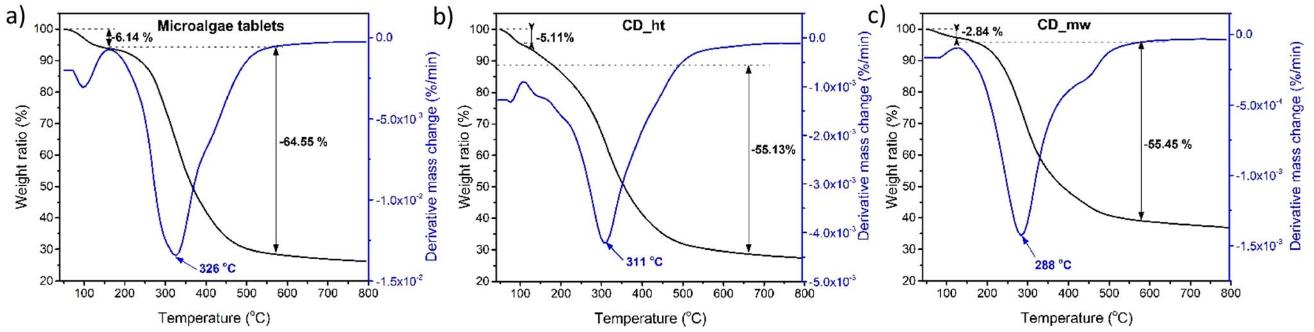

Fig. 8 TGA analysis of microalgal tablets (a), CD_ht (b) and CD_mw (c).

the presence of ZnO in the nanocomposite. However, the high-resolution O 1s XPS spectrum revealed the presence of 1.3% organic oxygen, which was assigned to CD_mw. The high-resolution XPS spectra of C 1s for ZnO_3CD_mw was fitted to eight different signals, which were described as followed: C=C, C–H, C–C, C–OH, C–O–C, C=O, O=C–OH, and CO_3^{2-}. In contrast, the signals in the C 1s region of the reference ZnO were deconvoluted into C–C, C–H, C–OH, C–O–C, C=O, and O–C=O peaks. The presence of carbon in ZnO_3CD_mw and the referenced ZnO could originate mostly from the zinc precursor–zinc acetate dihydrate. However, the presence of CD in the nanocomposite was also confirmed by other techniques, for example, PL spectra.

The SEM technique was used to determine the morphological characteristics of selected specimens. Fig. 10 shows images of ZnO, ZnO_3CD_ht, and ZnO_3CD_mw. The unmodified ZnO

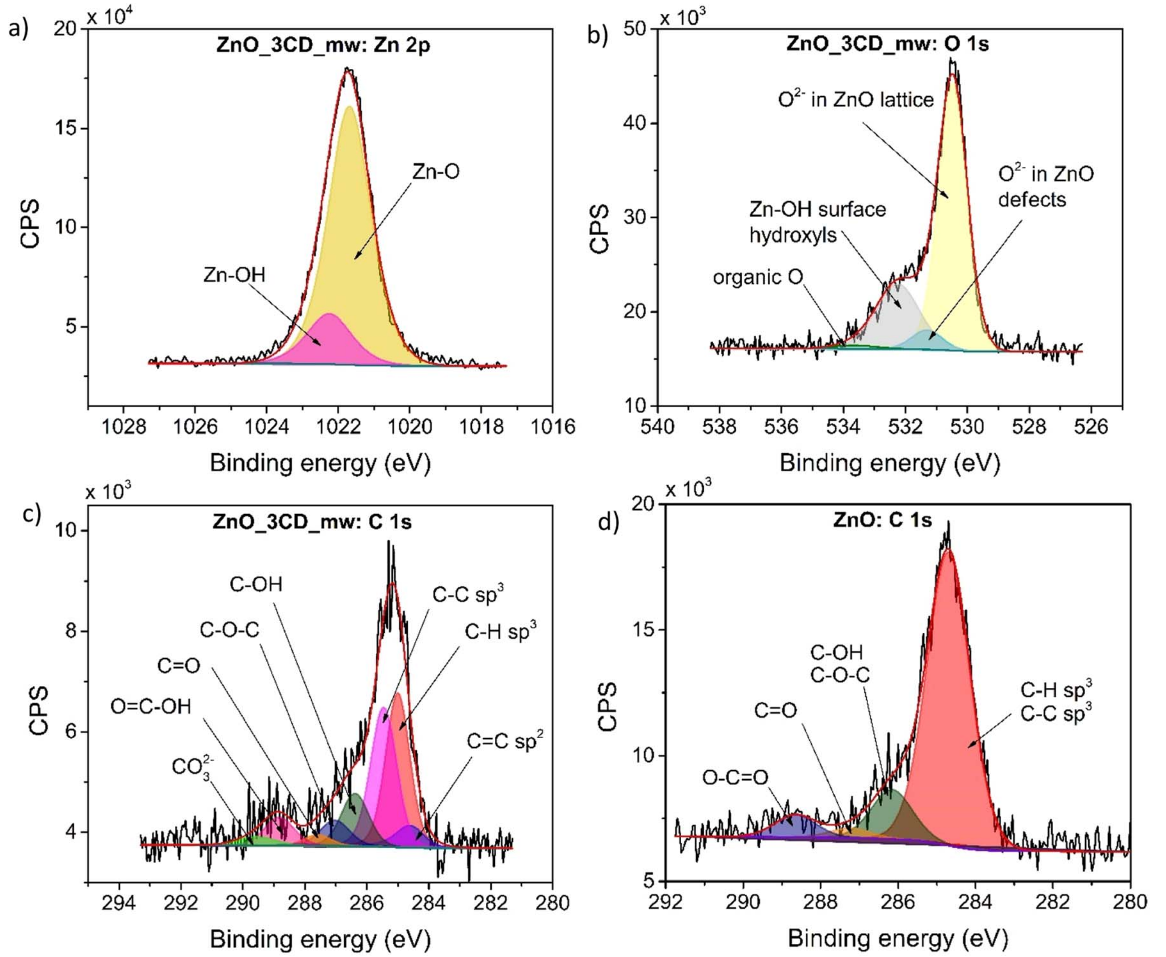

Fig. 9 High-resolution deconvoluted XPS spectra for Zn (a), O (b), C (c) of ZnO_3CD_mw, and for C of the reference ZnO sample (d).

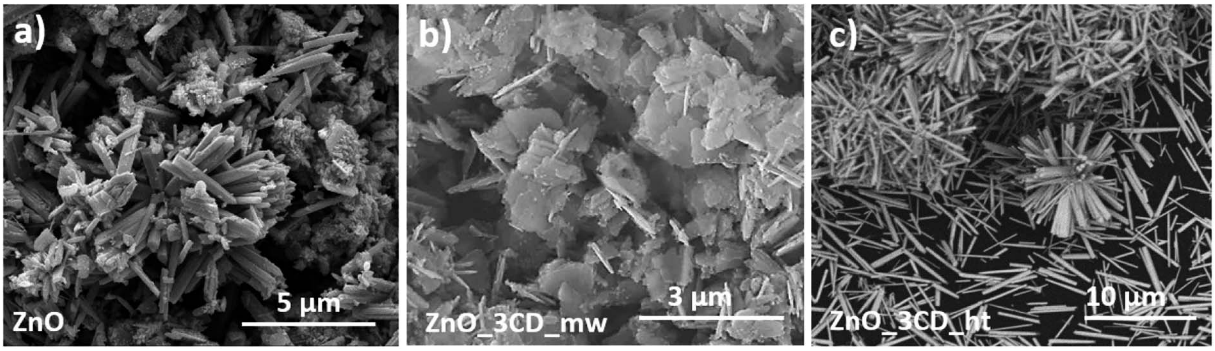

Fig. 10 SEM images of ZnO (a), ZnO_3CD_mw (b) and ZnO_3CD_ht (c).

shows a non-uniform matrix of nanocolumns with an average length of 2.24 μm and a thickness of 290 nm. Synthesis of ZnO in the presence of CD_ht resulted in the formation of uniform wires with a length of 1.14–6.24 μm (average 3.21 μm) and a thickness of 112–515 nm (average 287 nm). It is noteworthy that the sample ZnO_3CD_mw represents a 2D ZnO nanostructure with nanowalls with a width of 253–886 nm (average 503 nm) and a thickness of 28–87 nm (average 56 nm).

The specific surface area of ZnO and composites from the series ZnO-*x*CD were measured using the BET and were from 2.97 $m^2\ g^{-1}$ for ZnO and to 10.90 $m^2\ g^{-1}$ for ZnO_3CD_mw. The BET surface areas of the other samples are summarized in Table 2. In general, the CD presence increased the BET surface area of the composites. The increase in the BET surface area of ZnO-*x*CDs indicates that the presence of CD also enhances ZnO nanoparticle formation, which is supported by the XRD and SEM measurements. For the series of ZnO composites coupled with CD_mw, the highest BET surface area was obtained for the sample in the presence of 3% CD_mw during synthesis, while for the ZnO composites coupled with CD_ht, the highest BET surface area was obtained for the sample in the presence of 1.5% CD_mw during synthesis. The higher surface area enhances the incident light-harvesting, provides more active sites for micropollutants' adsorption on the surface, and thus, for ZnO_3CD_mw increases the photodegradation efficiency.[60]

The XRD diffraction patterns of all the samples in Fig. 11a exhibit the typical peak patterns of the ZnO wurtzite structure in the standard data (JCPDS 36-1451). The peaks at 2θ of 31.9°, 34.6°, 36.4°, 47.7°, 56.8°, 63.0°, 66.4°, 67.9°, 69.1°, 72.5°, and 76.9° correspond to the (100), (002), (101), (102), (110), (103), (200), (112), (201), (004) and (202) planes of ZnO. No other diffraction peaks related to CDs were observed in the ZnO_*x*CD nanocomposites because the diffraction intensity of the CDs peak is much lower than that of the peaks assigned to the ZnO structure. The diffraction peaks of the ZnO_0.75CD_ht, ZnO_0.75CD_mw, ZnO_3CD_ht, and ZnO_3CD_mw samples are shown in Fig. 11b. In all the aforementioned cases, the peaks shifted to the greater 2 theta degree values compared to those of bare ZnO. The use of CD_mw caused a greater shift in the diffraction peaks than the application of CD_ht. The XRD results indicated that the CDs caused changes in the ZnO crystal structure, which depended on the amount of CD and the preparation method. The lattice parameters calculated from the XRD spectra and the crystallite sizes of the obtained materials are summarized in Table 2. The lattice parameters of the samples characterized by shifted diffraction peaks were slightly lower than those of the reference ZnO. The lattice parameters were 3.245 Å for ZnO_3CD_mw and 3.241 Å for ZnO_0.75CD_mw, whereas that for unmodified ZnO was 3.253 Å. Additionally, ZnO_3CD_mw and ZnO_0.75CD_mw were characterized by significantly smaller particle size of approximately 34–38 nm in comparison to ZnO (49.4 Å). Previous studies have revealed that CDs may affect the crystal structure of ZnO.[35,61] Song *et al.* suggested that the shifting of diffraction peaks may originate from the interaction between ZnO and CDs.[62] The shift toward a higher angle of the peak related to

Table 2 CD content, synthesis method, BET surface area, lattice parameters ($a = b$, c, c/a ratio), average crystallite size, and energy bandgap of hybrid photocatalysts from the ZnO-*x*CD series

Sample name	CD content (%)	CD synthesis method	BET surface area ($m^2\ g^{-1}$)	Lattice parameters			Crystallite size (nm)	E_g (eV)
				$a = b$ (Å)	c (Å)	c/a		
ZnO	0	—	2.968 ± 0.015	3.253	5.210	1.6016	49.4	3.18
ZnO_3CD_mw	3.0	Microwave	10.900 ± 0.034	3.245	5.197	1.6015	34.3	3.19
ZnO_3CD_ht	3.0	Hydrothermal	3.061 ± 0.049	3.248	5.202	1.6016	48.6	3.10
ZnO_1.5CD_mw	1.5	Microwave	4.101 ± 0.053	3.252	5.209	1.6018	45.0	3.14
ZnO_1.5CD_ht	1.5	Hydrothermal	5.006 ± 0.059	3.251	5.207	1.6017	41.1	3.16
ZnO_0.75CD_mw	0.75	Microwave	3.753 ± 0.021	3.241	5.190	1.6014	38.5	3.16
ZnO_0.75CD_ht	0.75	Hydrothermal	2.601 ± 0.024	3.249	5.205	1.6020	45.4	3.18

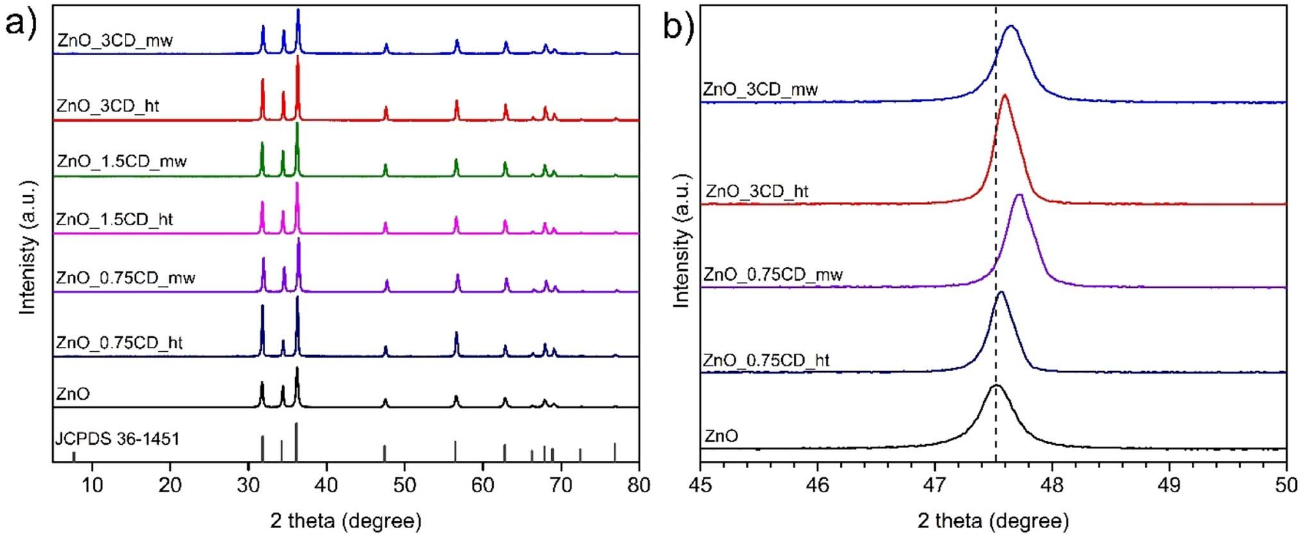

Fig. 11 (a) XRD pattern and (b) XRD pattern in 45°–50° 2 theta range of ZnO and ZnO_*x*CD nanocomposites.

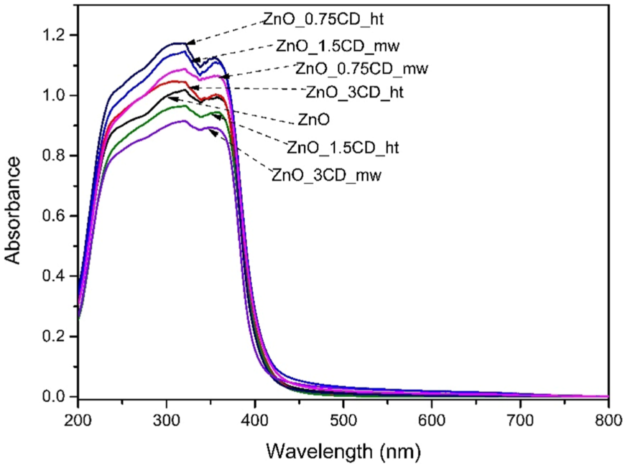

Fig. 12 UV-vis spectra of ZnO, ZnO-*x*CD nanocomposites.

ZnO crystalline plane was observed for metal-doped ZnO with a smaller cation than Zn^{2+}, *e.g.*, Fe-[63,64] or Mn- doped ZnO.[65,66] Fe and Mn were detected in both CD_ht and CD_mw aqueous solutions by ICP-OES analysis. This suggests that the shift of peaks on the XRD patterns of ZnO_*x*CD nanocomposites may be caused by Fe or Mn doping.

UV-vis diffuse reflection measurements were used to investigate the optical properties of the photocatalysts. The absorption spectra of the synthesized ZnO and the ZnO-*x*CD nanocomposites are shown in Fig. 12. The absorption peak for all samples was found to be between 350 and 365 nm, which is typical for ZnO according to previous studies.[67] The optical absorbance was calculated from the optical reflectance data using the Kubelka–Munk function ($\alpha = (1 - R)^2/2R$), where α and R are the absorption and diffuse reflectance coefficients, respectively.[68] According to the Kubelka–Munk function and the plot of $(\alpha h\nu)^{1/2}$ against the energy ($h\nu$), the bandgaps (E_g) of ZnO, ZnO_3CD_mw, ZnO_3CD_ht are estimated as 3.18, 3.19, and 3.10 eV, respectively (Fig. S2†).[69] The bandgap energy values of the other samples are summarized in Table 2, and each was characterized to be at a similar level. However, ZnO_3CD_ht was characterized by the lowest E_g value.

Subsequently, 2D PL spectroscopy was carried out at room temperature for ZnO, ZnO_3CD_ht, and ZnO_3CD_mw. The excitation–emission contour maps are shown in Fig. 13a–c. By varying the excitation wavelength from 300 to 450 nm, we observed that for the ZnO photocatalyst, the two highest emission intensity peaks were observed at 590 nm and 630 nm under excitation from 340 to 370 nm. For the ZnO_3CD_ht photocatalyst, the highest emission intensity peaks were observed at the same wavelength; however, for the first peak, this maximum was observed only under excitation at 370 nm, and the second peak was observed in the same range of excitation as for pure ZnO. Then, in the last map for ZnO_3CD_mw, we can also observe the same highest emission intensity peaks, but only under excitation at 370 nm. To compare the emission intensities of the analysed samples, the PL spectra at an excitation wavelength of 370 nm are shown in Fig. 13d. The PL intensities of ZnO_3CD_mw and ZnO_3CD_ht were lower than that of pure ZnO, demonstrating that the ZnO nanocomposites with CD exhibited improved optical properties. This is caused by the CDs, which act as electron traps to suppress the recombination of electron–hole pairs.

Next, the PL spectra of ZnO, ZnO_3CD_ht, and ZnO_3CD_mw were deconvoluted using Gaussian fitting. We can observe emissions in different wavelength regions in the PL spectra depending on the analysed sample, which is due to the presence of defect states in ZnO. All three types of examined nanostructures, ZnO (Fig. 13e), ZnO_3CD_ht (Fig. 13f), and ZnO_3CD_mw (Fig. 13g) show common visible light emission peaks in the following ranges: 500–530 nm (blue–green region), 560–580 (green region), 630–640 (orange region) and 635–700 (red region), and additional samples modified with CD revealed

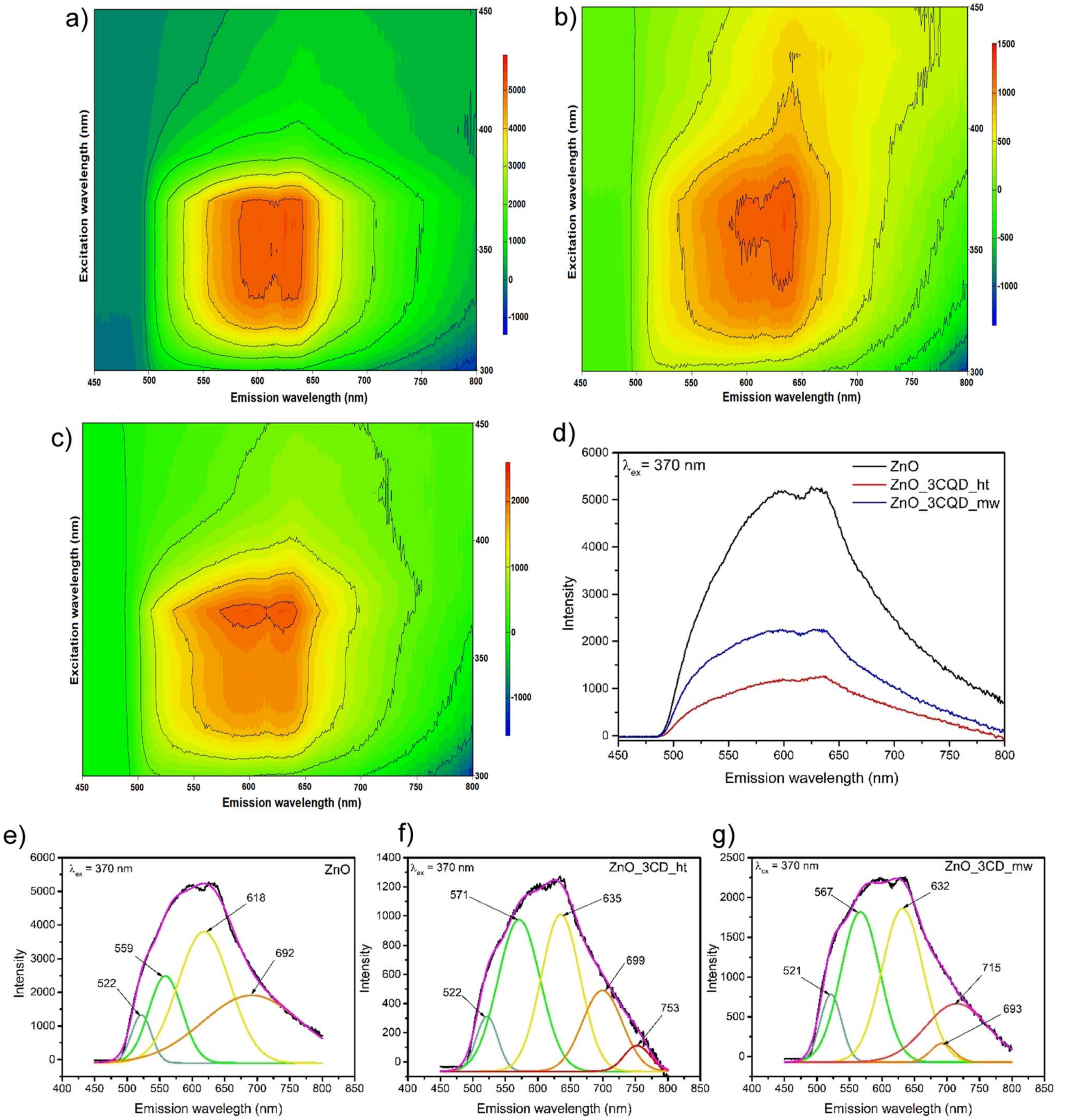

Fig. 13 2D PL spectra under the excitation wavelengths range from 300–450 nm of (a) ZnO, (b) ZnO_3CD_ht, (c) ZnO_3CD_mw and (d) PL spectra of ZnO, ZnO-3CD_ht, and ZnO_3CD_mw nanocomposites under excitation wavelength 370 nm, (e–g) deconvolution of PL spectra of ZnO, ZnO_3CD_ht and ZnO_3CD_mw.

an additional peak at 710–760 (high-red region). Quantification of the intensities of the components (peak area) depends on the type of sample, and the exact percentages are given in Table S1.† These results clearly show the contributions originating from various point defects in the ZnO structure. According to recent studies, the blue–green emission peak represents the electronic transition from E_C to O_{Zn} or from O_V^+ to E_V.[70] The second emission peak in the green region can be assigned to the electronic transition from E_C to V_O^{++}.[70,71] The peaks in the orange and red regions are due to the electronic transition from Zn_i to O_i.[71] The additional high-red peak appearing in the ZnO samples modified by CDs can be attributed to electronic transition involving deep-level states, such as oxygen defects. To date, different options have been reported for explaining transitions in this region.[72] Galdámez-Martinez *et al.*[73] assigned the emission at 750 nm to electronic transition from V_o below C_B ($C_B \rightarrow V_o$); while the emission at 780 nm was assigned to electronic transition O_i above V_B, resulting in ($O_i \rightarrow V_B$). Kumar

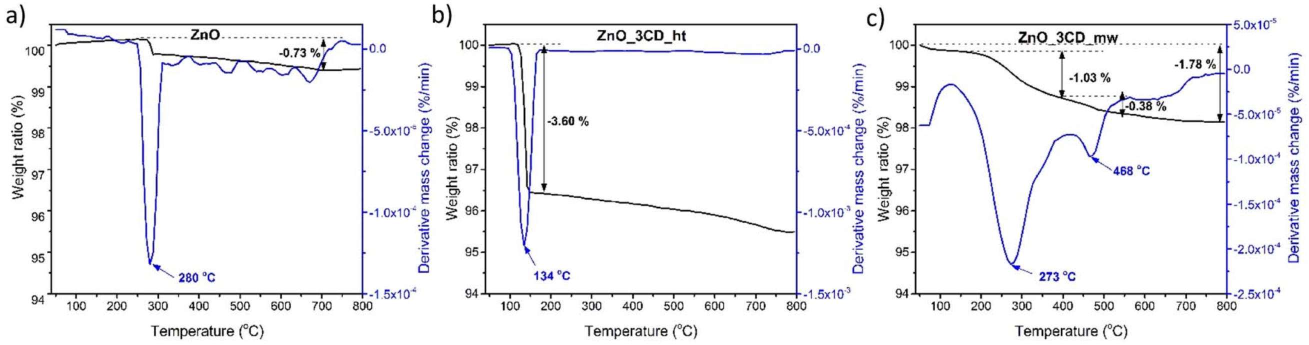

Fig. 14 TGA analysis of ZnO (a), ZnO-3CD_ht (b), and ZnO_3CD_mw (c) nanocomposites.

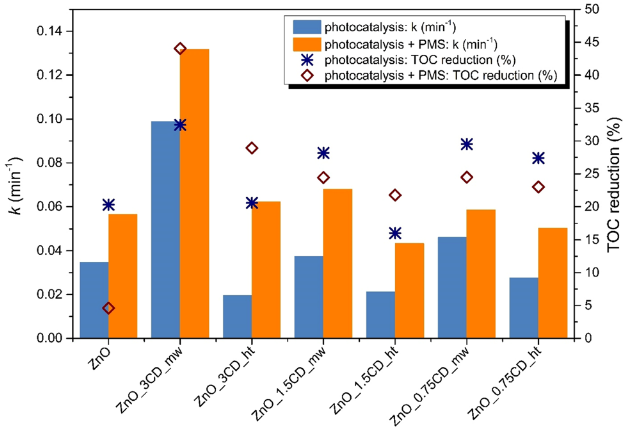

Fig. 15 Comparison of degradation rate and mineralization of CBZ in the presence of the photocatalyst from the ZnO_*x*CD series. Experimental conditions: CBZ initial concentration: 14 mg dm^{-3}, V =25 cm^3, photocatalyst: 0.5 g dm^{-3}, irradiation time = 60 min.

et al.[74] assigned red emission of 760 nm to V_o below the C_B ($Zn_i \rightarrow V_o$). Anjum *et al.*[71] proposed the assignment of the following electronic transitions $C_B \rightarrow V_o$, $V_o \rightarrow V_B$, or $H_i \rightarrow V_o$. In the case of our study, we can assume that the modification of ZnO with CDs resulted in a variety of changes in electronic transitions, causing the presence of different levels of defects. These results coincide with XPS and XRD findings.

TGA was performed to study the thermal degradation profile of ZnO and the selected ZnO-*x*CD nanocomposites with the highest CD content (Fig. 14). For ZnO, a slight increase in the mass was observed upon increasing the temperature to 272 °C, followed by a stepwise weight loss in the temperature range of 272–288 °C. This confirms the presence of trace amounts of $Zn(OH)_2$, which is transformed into ZnO at approximately 280 °C.[75,76] The thermograms of the ZnO_3CD_ht and ZnO_3CD_mw composites differed significantly from each other. In the case of ZnO_3CD_ht, a one-step mass loss of 3.6% was recorded in the temperature range of 119–157 °C. In contrast, the total mass loss of ZnO_3CD_mw was 1.78%, which was almost two times smaller than that of ZnO_3CD_ht. In addition, ZnO_3CD_mw was characterized by a three-step thermal degradation: the first step of degradation was observed in the range of 50–81 °C and was 0.11%, the main stage with weight loss of 1.03% was in 157–410 °C, and the last degradation step at 140–540 °C was 0.38%.

3.3. Photocatalytic activity of ZnO-*x*CD nanocomposites

The photocatalytic performance of the ZnO-*x*CD composites was evaluated for the degradation of the selected micropollutant, CBZ, in water under UV-vis irradiation. The Langmuir–Hinshelwood (LH) model is commonly used to express the first-order kinetic rate constant during photocatalytic degradation, where the reaction rate is independent of C_0. In the simplified model, it was hypothesized that adsorption achieved adsorption–desorption equilibrium, and in our case, illumination was started after 30 min of constant stirring in the dark. Additionally, a preliminary study of the CBZ adsorption process onto photocatalysts showed that this process was negligible, and adsorption–desorption equilibrium was achieved after half an hour of mixing in the dark, and no more than 4% of CBZ was adsorbed on each examined photocatalyst.

The examination of series ZnO-*x*CD composites were seen at a photocatalyst dose of 0.5 g dm^{-3}, temperature of 20 °C, and neutral pH value. First, the removal of CBZ using a photolytic process was investigated. The results in Fig. S3† show that this process was not efficient, and the degradation rate was very low: after one hour of irradiation, only 13% of CBZ was degraded, and this process did not cause CBZ mineralization. The effectiveness of CBZ degradation was investigated in the presence of PMS under UV-vis irradiation. This process enabled the degradation of the parent compound; 100% of CBZ was degraded after one hour, but the mineralization was insufficient, and only 13% TOC reduction was observed. The other trend was noticed in the photocatalytic process, where the efficiency of CBZ removal was high by a simple photocatalytic process being accelerated in the presence of PMS, bringing a higher first-order kinetic rate constant and a higher mineralization process. The results shown in Fig. S3b† indicates that photolytic and photocatalytic processes, as well as those supported by PMS, have a good correlation with the first-order reaction kinetics ($R^2 >$ 0.98) and for better clarity of the further experiments, only kinetic rate constant (k) values will be expressed in the next results.

Fig. 15 shows a comparison between ZnO and ZnO-*x*CD for the photodegradation of CBZ by simple photocatalysis and PMS

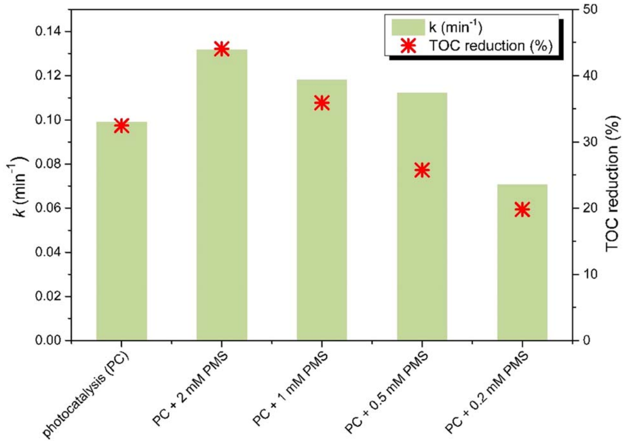

Fig. 16 Influence of PMS concentration on degradation rate and mineralization of CBZ in the presence of ZnO_3CD_mw under UV-vis irradiation. Experimental conditions: CBZ initial concentration: 14 mg dm^{-3}, $V = 25$ cm^3, photocatalyst: 0.5 g dm^{-3}, PMS concentration = 0.2–2 mM, and irradiation time = 60 min.

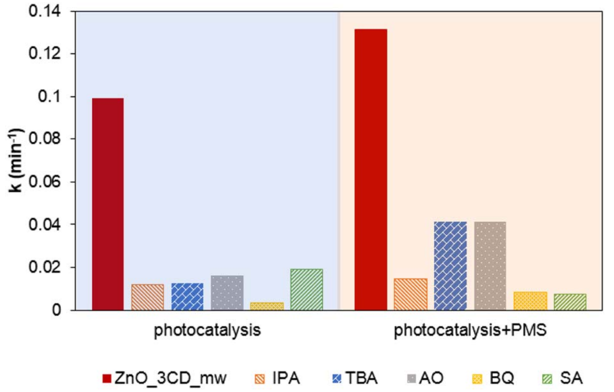

Fig. 17 Effect of scavengers on CBZ degradation using ZnO_3CD_mw by photocatalytic process and photocatalytic process supported by PMS on the first-order kinetic rate constant in the presence of isopropanol (IPA), *tert*-butanol (TBA) ammonium oxalate (AO), benzoquinone (BQ) and sodium azide (SA). Experimental conditions: CBZ initial conc.: 14 mg dm^{-3}, $V = 25$ cm^3, photocatalyst: 0.5 g dm^{-3}, PMS conc. = 0–2 mM, irradiation time = 60 min.

activation. Among all the composites of ZnO decorated with CD_mw and CD_ht, considering the dependence of CD content on the photocatalytic activity of ZnO-*x*CD composites, ZnO synthesized with 3% microwave CDs, exhibited the highest photocatalytic activity. The first-order kinetic rate constant was 2.85 times higher, and mineralization was 12% higher in the presence of ZnO_3CD_mw than in the presence of ZnO. An improvement in the photocatalytic activity was also observed in the presence of ZnO_1.5CD_mw (at 8% higher *k*-value and 8% higher mineralization) and ZnO_0.75CD_mw (at 33% higher *k*-value and 9% higher mineralization). However, it is evident that the photocatalytic activities expressed by the first-order kinetic rate constant for the samples from the series of ZnO_*x*CD_ht are lower than those of pure ZnO. On the other hand, the mineralization for the ZnO_3CD_ht sample was at the same level as the mineralization achieved for ZnO, while for the samples ZnO_1.5CD_ht and ZnO_0.75CD_ht, mineralization was 4% lower and 7% higher, respectively.

In addition to the photocatalytic process (PC system), the degradation performances of the system supported by the presence of PMS (PC/PMS system) towards CBZ degradation was explored to accelerate PMS activation to generate highly reactive $SO_4^{\bullet-}$. The photocatalytic performance of this system for CBZ degradation was remarkably enhanced by the composite material under the simultaneous action of PMS and light irradiation, as shown in Fig. 16. The highest increase in first-order kinetic rate constant of the PC/PMS system compared to the PC system was observed for the ZnO_3CD_ht, where *k* value increased until 3.17 times. Subsequently, a significant improvement in the *k* value was also observed for ZnO_1.5CD_ht and ZnO_0.75CD_ht by 100% and 80%, respectively. On the other hand, the presence of CD_mw in the composites did not accelerate this process to a higher level than that of pure ZnO. It can be concluded that the CDs obtained by the hydrothermal method caused a higher PMS activation than the CDs obtained by the microwave method. In contrast, the mineralization in the presence of ZnO_3CD_mw was the highest, reaching 44%. This photocatalyst (ZnO_3CD_mw) showed the best activity in the photocatalytic process and the highest mineralization in the PC/PMS system.

PMS addition significantly improved the photocatalytic activity of ZnO_*x*CD, as expressed by the first-order kinetic rate constant and enhanced the mineralization for the degradation of CBZ (Fig. 16). It is noteworthy that the photocatalytic mineralization of CBZ by ZnO was almost completely inhibited by PMS addition, whereas in the presence of ZnO_3CD_mw, the addition of PMS caused an enhancement of CBZ mineralization by 37.5% compared with the value obtained in the simple photocatalytic process. Considering promising results of PMS action in the presence of ZnO_3CD_mw, in the next step of research, the influence of PMS dose on the CBZ removal by ZnO_3CD_mw was examined. The results of this experiment are shown in Fig. 16. The first-order kinetic rate constant of CBZ degradation increased by 33%, 19%, and 13% in the presence of 2 mM, 1 mM and 0.5 mM of PMS. In contrast, the process decreased by 29% by adding 0.2 mM PMS. The dose of PMS also influenced the mineralization process, and at doses of 2 mM and 1 mM, mineralization was accelerated by 35 and 11%, respectively. Mineralization was inhibited by the presence of PMS (0.5 mM PMS and 0.2 mM PMS up to 29 and 40%, respectively, compared with the lower PMS-containing photocatalytic system (with 2 mM PMS)). Therefore, 2 mM PMS was selected for further investigation.

In the photocatalytic process, several highly reactive species (*e.g.*, h^+, $^{\bullet}OH$, e^-, $O_2^{\bullet-}$, and $^1O_2$) may be produced and can react with CBZ.[77,78] The photocatalytic activation of PMS results in the formation of sulphate radicals ($SO_4^{\bullet-}$). Isopropanol (IPA) was chosen as the radical scavenger for $^{\bullet}OH$ and $SO_4^{\bullet-}$, whereas, *tert*-butanol (TBA) can only inhibit $^{\bullet}OH$ radicals.[79] Additionally, the contribution of h^+, $O_2^{\bullet-}$, and $^1O_2$ was also examined by the action of AO, BQ, and SA, respectively. As shown in Fig. 17, the impact of the addition of BQ was the highest, and the removal

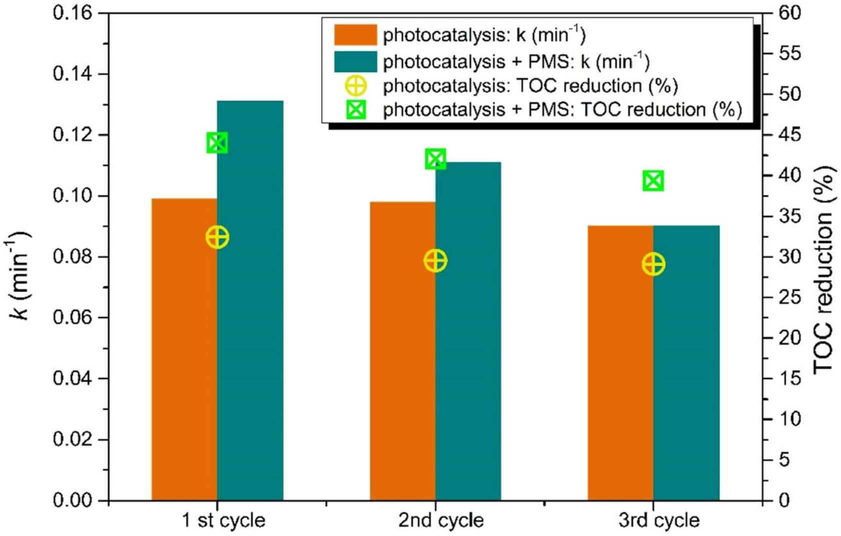

Fig. 18 Comparison of the first-order kinetic rate constant and TOC reduction in the recycling tests of the ZnO_3CD_mw catalyst for the degradation of CBZ in the photocatalytic process and supported by PMS. Experimental conditions: CBZ initial concentration: 14 mg dm^{-3}, $V = 25$ cm^3, photocatalyst: 0.5 g dm^{-3}, PMS conc. = 2 mM; irradiation time = 60 min.

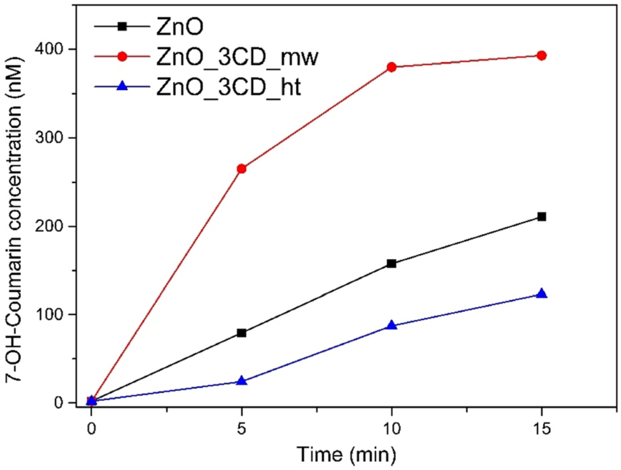

Fig. 19 Production of 7-hydroxycoumarin (monitored by fluorescence emission) in suspensions of bare ZnO, ZnO_3CD_mw, and ZnO_3CD_ht under UV-vis irradiation. Experimental conditions: [catalyst] = 0.5 g dm^{-3}, [coumarin]$_0$ = 50 μM.

of CBZ was reduced with a decrease in the *k* value by 93.5%. This result suggests that $O_2^{\bullet-}$ radicals have a major effect on the photocatalytic degradation in the presence of ZnO_3CD_mw. Nevertheless, with the addition of other studied scavengers – IPA, TBA, AO, and SA, the degradation rate of CBZ decreased by approximately 80% compared to the control system. These results suggest that other radical species were also generated during the photocatalytic process and reacted with CBZ. In the photocatalytic process supported by PMS, it was clearly demonstrated that in the presence of IPA, CBZ degradation was inhibited by 89%, whereas in the presence of TBA, the process was inhibited by 68%. Therefore, the role of $SO_4^{\bullet-}$ radicals in CBZ degradation was demonstrated. Furthermore, $O_2^{\bullet-}$ and $^1O_2$ played important roles in the degradation of CBZ by the PC/PMS system. Comparing the degradation of CBZ in the presence of BQ – agent responsible for the assessment of $O_2^{\bullet-}$ contribution, the first-order kinetic rate constant was 2.5 times higher than that in the PC/PMS system, indicating that other species became more significant. The other trend was observed in the experiments of CBZ degradation in the presence of SA, indicating the contribution of $^1O_2$ action, where the first-order kinetic rate constant decreased by 62% compared to the PC system with the PC/PMS system. This observation proves the major contribution of $^1O_2$ to the removal of organic pollutants, and it has also been reported in other studies on PMS and PS activation.[80] The activation PMS through a $^1O_2$-dominated non-radical pathway have been demonstrated in the presence of carbonaceous materials, including carbon nanotubes (CNTs), carbon spheres, nanodiamond, graphene oxide (GO), reduced graphene oxide (rGO), and biochar.[81] In the present study, $^1O_2$-dominated non-radical pathway was found to be highly important for ZnO modified by CDs. PMS activation by ZnO_3CD_mw photocatalyst can be expressed by consecutive reactions from electron/hole generation (eqn (1)). Firstly, the reduction of PMS can generate $SO_4^{\bullet-}$ (eqn (2)), which can react with pollutants and/or cause the formation of $^\bullet OH$, as the result of $SO_4^{\bullet-}$ reaction with OH^- (eqn (3)).[82]

$$\text{ZnO\_3CD\_mw} + h\nu \rightarrow h^+ + e^- \tag{1}$$

$$HSO_5^- + e^- \rightarrow SO_4^{\bullet-} + OH^- \tag{2}$$

$$OH^- + SO_4^{\bullet-} \rightarrow {}^\bullet OH + SO_4^{2-} \tag{3}$$

Secondly, singlet oxygen can be generated *via* O_2 dependent pathway as a consecutive reaction from $O_2^{\bullet-}$ produced by oxygen reduction (eqn (4)) *via* reaction with $^\bullet OH$, H^+, and/or h^+ (eqn (5) and (6)).

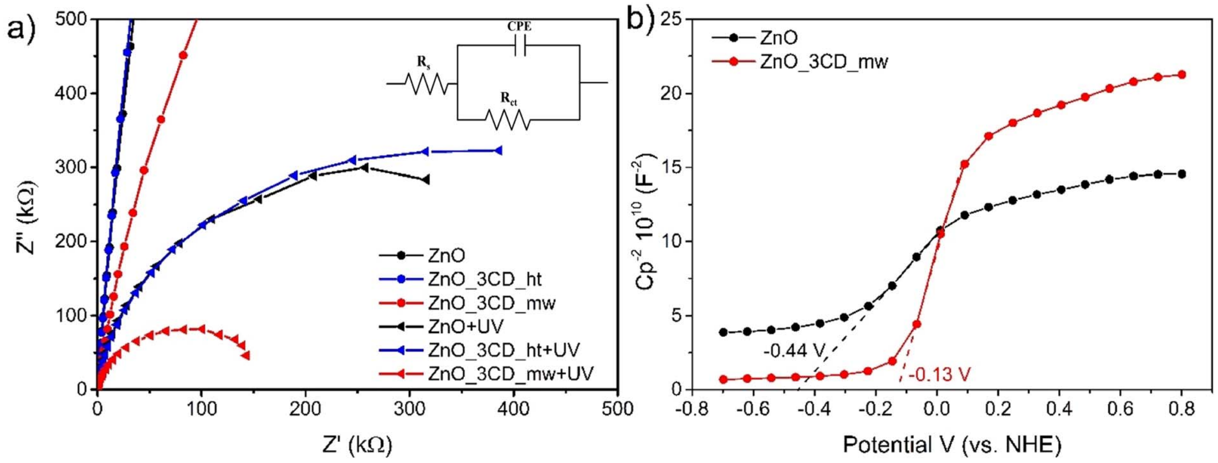

Fig. 20 (a) Nyquist plots of ZnO, ZnO_3CD_mw, and ZnO_3CD_ht without and with light (λ = 380–390 nm, [Na_2SO_4] = 1 M), and (b) Mott–Schottky plots of ZnO and ZnO_3CD_mw.

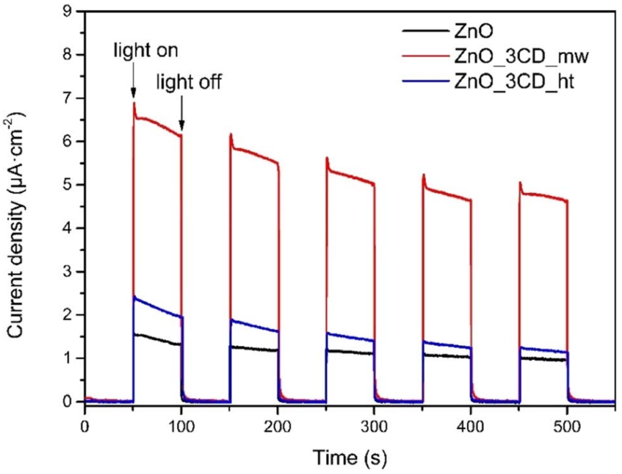

Fig. 21 Transient photocurrent responses of ZnO, ZnO_3CD_mw, and ZnO_3CD_ht (λ = 380–390 nm, [Na_2SO_4] = 1 M).

$$O_2 + e^- \rightarrow O_2^{\bullet -} \quad (4)$$

$$O_2^{\bullet -} + {}^{\bullet}OH \rightarrow {}^1O_2 + {}^-OH \quad (5)$$

$$2O_2^{\bullet -} + 2H^+ \rightarrow {}^1O_2 + H_2O \quad (6)$$

$$O_2^{\bullet -} + h^+ \rightarrow {}^1O_2 \quad (7)$$

Thirdly, singlet oxygen can be formed through photogenerated holes (h^+)-dependent pathway by PMS oxidation and consecutive reaction with water (eqn (8) and (9)).[83]

$$HSO_5^- + h^+ \rightarrow SO_5^{\bullet -} + H^+ \quad (8)$$

$$2SO_5^{\bullet -} + 2H_2O \rightarrow {}^1O_2 + 1.5\ HSO_4^- \quad (9)$$

Based on the aforementioned results, different types of active species play certain roles in the CBZ degradation reactions of the PC and PC/PMS systems. In general, the $O_2^{\bullet -}$ was the main active species during the photocatalytic process, whereas in the process supported by PMS, a high role of $^1O_2$ was also observed. Furthermore, $SO_4^{\bullet -}$ radicals participated in the photocatalytic process assisted by PMS.

The important factor in photodegradation for actual application is the recycling ability of the photocatalysts. To study the stability of the selected photocatalyst with the optimal amount of CDs, the recycling experiment was carried out, as shown in Fig. 18. The photocatalytic degradation of CBZ by the ZnO_3CD_mw photocatalyst exhibited no significant decrease in the first-order kinetic rate constant or TOC reduction. The degradation ability expressed by *k* decreased only by 1.2% after the second run and 8.9% after the third run, while TOC values indicate that the mineralization process was inhibited by 9.1% and 10.3%. These results indicate that ZnO_3CD_mw has good recyclability for photocatalytic processes. However, a slight reduction in the photocatalytic process assisted by PMS was observed. The first-order kinetic rate constant decreased after the third run to the level revealed by a conventional photocatalytic process. Meanwhile, TOC reduction was higher by about 12% in each process assisted by PMS compared with the photocatalytic process.

Moreover, the influence of selected anions (Cl^-, HCO_3^-, and NO_3^-) as well as the use of artificial marine water as the most likely concentrated ions in environmental water was investigated. These factors are known to reduce photocatalytic efficiency, therefore, the influence of ions was assessed for the selected concentration of 10 mM to examine the effect of single ions, as well as for marine water, as shown in Fig. S4(a).† A slight inhibition of CBZ photocatalytic degradation was observed in the presence of each ion, and the first-order kinetic rate constant decreased the most in the presence of Cl^-, where it was inhibited by 13.8%, whereas the presence of HCO_3^- resulted in 10.4% inhibition. Less significant inhibition was observed for NO_3^-, where the first-order kinetic rate constant decreased by only 2.1%. The extreme salinity conditions revealed by the marine water environment resulted in a 26.1%

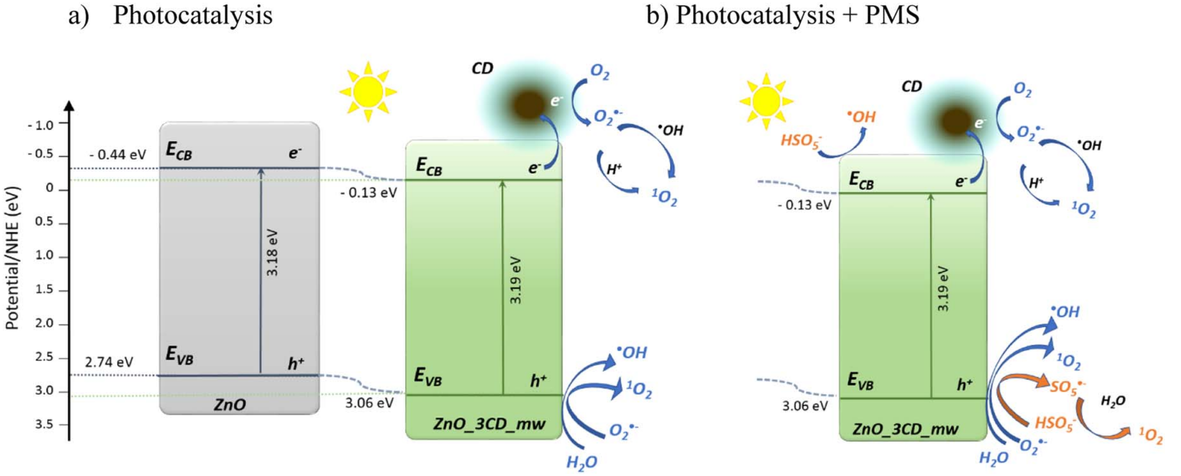

Fig. 22 Schematic photogeneration of charges in the ZnO_3CD_mw nanocomposite combined with the possible reaction mechanism of photocatalysis (a), and photocatalysis supported by PMS (b).

decrease in the first-order kinetic rate constant. Further, the effect of pH on CBZ removal was examined, selected initial pH concentrations equal 3.1, 6.6 (without adjustment) and 9.0 were considered in the reaction mixture, as shown in Fig. S4(b).† CBZ with two pKa values (2.3 and 13.9)[84] exists in the neutral form at all examined pH values. The CBZ removal was at the same level at pH = 9, with a decrease of k by only 0.9% compared with k observed at a natural pH of 6.6, while the process at pH 4.1 revealed a decrease in k by 56.9%. The inhibition of the photocatalytic process under acidic conditions can be explained by the corrosion of the photocatalyst, as previously reported by Ayu *et al.*[85]

3.4. Discussion on the enhanced photocatalytic activity of ZnO_*x*CD composites

The photocatalytic efficiency of ˙OH radical production was compared by monitoring coumarin-OH adduct (7-hydroxycoumarin) generation in the presence of selected photocatalysts (ZnO, ZnO_3CD_mw, and ZnO_3CD_ht). The results are shown in Fig. 19. The production of coumarin-OH with ZnO_3CD_mw was the highest among the photocatalysts. The generation of ˙OH radicals on the sample modified by CD_mw was up to 3.3 times higher compared with ZnO after 5 min of irradiation. On the other hand, the modification of ZnO by CD_ht inhibited the generation of ˙OH radicals by 70% after 5 min of reaction compared to ZnO. The ZnO_3CD_mw sample exhibits a maximum formation rate of ˙OH, which is in line with the best photocatalytic activity demonstrated by earlier CBZ degradation experiments.

Electrochemical impedance spectroscopy (EIS) was performed under dark and light conditions and Nyquist plots of the selected samples are shown in Fig. 20a. The arc radius in the EIS Nyquist plot denotes the charge transfer resistance (R_{ct}) at the electrode/electrolyte interface. Under dark conditions, the Nyquist plots for all samples consisted of a straight line in the low-frequency region. However, under light irradiation, the Nyquist plots exhibited a significantly lower arc radius, which indicates a lower R_{ct}. Equivalent circuit fitting was performed to estimate the R_{ct} values of the analysed samples. The experimental data fit well with the simple Randles equivalent circuit shown in the inset of Fig. 20a, where R_s is the solution resistance and CPE is a constant phase element. The R_{ct} values of ZnO, ZnO_3CD_ht, and ZnO_3CD_mw were 671, 717, and 180 kΩ, respectively. In this study, ZnO_3CD_mw was characterized by the lowest R_{ct} among the analysed samples under light irradiation, which resulted in the highest photocatalytic decomposition of CBZ and PMS activation.

Transient photocurrent measurements for the ZnO, ZnO_3CD_mw, and ZnO_3CD_ht photocatalysts were performed, and the curves with the response of current density *versus* time are presented in Fig. 21. Experiments were run with several on/off cycles with an intermittent LED light source in a 1 M Na_2SO_4 aqueous solution.[86] It is observed that all the examined photocatalysts exhibit a quick response to the on–off cycles of the incident light, and the current density samples of ZnO modified by CDs show an enhancement compared with that of bare ZnO. ZnO_3CD_mw exhibited the largest photocurrent density of *ca.* 6.2 μA cm^{-2}, which is five times higher than that of ZnO, while ZnO_3CD_ht displays an approximately 30% higher photocurrent density than that of ZnO. The decrease in the photocurrent response in the second cycle compared with the first response for ZnO_3CD_mw and ZnO_3CD_ht seems to be negligible, as the response is stable and higher than that of ZnO observed in the last two cycles.

Based on the above studies, a possible mechanism for CBZ over the ZnO_3CDs_mw hybrid nanomaterial is proposed in Fig. 22. The enhancement effect of CDs in this system is mainly attributed to the action as an electron reservoir for hindering the recombination, but also to the controllable band position adjustment that was observed for the ZnO_3CDs_mw hybrid system. The mechanism for the enhancement was determined by analysing the coupled modes of the CDs at the interface of

ZnO as a result of the generation of reactive oxygen species. As shown in Fig. 22a, the pure ZnO with a band gap equal $E_g = 3.18$ eV, has the conduction band edge and valence band edge calculated to be −0.44 and 2.74 eV (*vs.* normal hydrogen electrode (NHE)), respectively. According to the Mott–Schottky analysis (Fig. 20b), after synthesis in the presence of CD_mw, the adjustment of the band structure was observed through changes in the inner environment of the ZnO crystals. Consequently, the conduction band bottom and valence band top were equal −0.13 and 3.06 eV, respectively. Furthermore, based on the determined V_B and C_B values of semiconductors, we can advise that various types of ROS are generated through photoexcitation.[87] The V_B values of ZnO and ZnO_3CD_mw (2.74 and 3.06 eV, respectively) were more positive than $E_{0(\mathrm{OH})^{\bullet}/\mathrm{OH}^{-}}$ (2.38 eV *vs.* NHE) and the C_B values of them (−0.44 and −0.13 eV, respectively) were negative than $E_{0(\mathrm{O_2/O_2^{\bullet-}})}$ (−0.046 eV *vs.* NHE). It is worth noting that the shifting of the band edge position before and after the modification of ZnO influenced the generation of reactive species, such as revealed by experiments on coumarin oxidation, which showed differences in $^{\bullet}$OH production. Additionally, in the presence of PMS, other species could be generated, as proven by experiments in the presence of scavengers with the major role of $^1O_2$ in CBZ degradation through the PC/PMS system.

4. Conclusions

Novel CDs were synthesized for the first time by the hydrothermal and microwave-assisted method from bio-delivered source of the algae *Chlorella pyrenoidosa*. The detailed studies confirmed that prepared CDs were multi-doped with nonmetals N, S and P, as well as metals, including higher contents of Ca, Mg, K, Na, and also Fe and Mn, which resulted in a shift of peaks in XRD and confirmed doping of ZnO. Multi-doped CDs revealed good fluorescence properties with red shift present and an average size of 23 nm and 68 nm for dots obtained by hydrothermal and microwave-assisted methods, respectively.

These nanomaterials were used in the synthesis of a series of ZnO-*x*CD photocatalysts using a simple solvothermal technique. Detailed studies using X-ray diffraction, TEM, BET, FTIR, XPS, UV-vis, and PL confirmed the crystal structure, chemical composition, and optical properties. The as-prepared ZnO_*x*CD_mw effectively degraded CBZ in water under UV-vis irradiation. The photocatalyst with 3% CD content obtained by microwave-assisted method showed the highest CBZ first-order degradation rate of 0.099 min^{-1}, and mineralization revealed by TOC reduction of 32.5% under UV-vis light. This study proved that ZnO-*x*CD composites can efficiently activate PMS to generate $SO_4^{\bullet-}$, $^{\bullet}$OH, and $^1O_2$. ZnO_3CDs_mw exhibited high stability in the subsequent photocatalytic reactions. In addition, a PMS-assisted process was investigated, and the activation of radical species by the CDs was demonstrated.

Conflicts of interest

There are no conflicts to declare.

Acknowledgements

Financial support of these studies from Gdańsk University of Technology by the DEC-6/2021/IDUB/II.2/Sc/035336 grant under the SCANDIUM-'Excellence Initiative-Research University' program is gratefully acknowledged.

References

1 Z. Guo, D. Kodikara, L. S. Albi, Y. Hatano, G. Chen, C. Yoshimura and J. Wang, Photodegradation of organic micropollutants in aquatic environment: importance, factors and processes, *Water Res.*, 2023, **231**, 118236, DOI: 10.1016/j.watres.2022.118236.

2 R. Andreozzi, R. Marotta, G. Pinto and A. Pollio, Carbamazepine in water: persistence in the environment, ozonation treatment and preliminary assessment on algal toxicity, *Water Res.*, 2002, **36**, 2869–2877, DOI: 10.1016/S0043-1354(01)00500-0.

3 Â. Almeida, A. M. V. M. Soares, V. I. Esteves and R. Freitas, Occurrence of the antiepileptic carbamazepine in water and bivalves from marine environments: a review, *Environ. Toxicol. Pharmacol.*, 2021, **86**, 103661, DOI: 10.1016/j.etap.2021.103661.

4 M. Mezzelani, L. Peruzza, G. d'Errico, M. Milan, S. Gorbi and F. Regoli, Mixtures of environmental pharmaceuticals in marine organisms: mechanistic evidence of carbamazepine and valsartan effects on *Mytilus galloprovincialis*, *Sci. Total Environ.*, 2023, **860**, 160465, DOI: 10.1016/j.scitotenv.2022.160465.

5 T. Bi, Z. Du, S. Chen, H. He, X. Shen and Y. Fu, Preparation of flower-like ZnO photocatalyst with oxygen vacancy to enhance the photocatalytic degradation of methyl orange, *Appl. Surf. Sci.*, 2023, **614**, 156240, DOI: 10.1016/j.apsusc.2022.156240.

6 A. Sulowska, A. Fiszka Borzyszkowska, K. Cysewska, K. Siwińska-Ciesielczyk, K. Nikiforow, G. Trykowski and A. Zielińska-Jurek, The effect of PEDOT morphology on hexavalent chromium reduction over 2D TiO_2/PEDOT photocatalyst under UV-vis light, *Mater. Chem. Phys.*, 2023, **299**, 127430, DOI: 10.1016/j.matchemphys.2023.127430.

7 R. Li, S. Braekevelt, J. L. N. De Carfort, S. Hussain, U. E. Bollmann and K. Bester, Laboratory and pilot evaluation of aquaporin-based forward osmosis membranes for rejection of micropollutants, *Water Res.*, 2021, **194**, 116924, DOI: 10.1016/j.watres.2021.116924.

8 A. Fiszka Borzyszkowska, A. Pieczyńska, A. Ofiarska, W. Lisowski, K. Nikiforow and E. M. Siedlecka, Photocatalytic degradation of 5-fluorouracil in an aqueous environment via Bi–B co-doped TiO_2 under artificial sunlight, *Int. J. Environ. Sci. Technol.*, 2020, **17**, 2163–2176, DOI: 10.1007/s13762-019-02604-z.

9 L.-H. Kao, K.-S. Chuang, H. N. Catherine, J.-H. Huang, H.-J. Hsu, Y.-C. Shen and C. Hu, MoS_2-coupled coniferous ZnO for photocatalytic degradation of dyes, *J. Taiwan Inst. Chem. Eng.*, 2023, **142**, 104638, DOI: 10.1016/j.jtice.2022.104638.

10 M. Shalahuddin Al Ja'Farawy, K. Kusumandari, A. Purwanto and H. Widiyandari, Carbon quantum dots supported zinc oxide (ZnO/CQDs) efficient photocatalyst for organic pollutant degradation – a systematic review, *Environ. Nanotechnol., Monit. Manage.*, 2022, **18**, 100681, DOI: **10.1016/j.enmm.2022.100681**.

11 L. Dejam, S. Kulesza, J. Sabbaghzadeh, A. Ghaderi, S. Solaymani, S. Tălu, M. Bramowicz, M. Amouamouha, A. hossein S. shayegan and A. hossein Sari, ZnO, Cu-doped ZnO, Al-doped ZnO and Cu–Al doped ZnO thin films: advanced micro-morphology, crystalline structures and optical properties, *Results Phys.*, 2023, **44**, 106209, DOI: **10.1016/j.rinp.2023.106209**.

12 N. R. Khalid, M. Sabir, F. Ali, M. B. Tahir, M. A. Javid, N. A. Niaz, R. Ahmed, M. Rafique, M. Imran and M. A. Assiri, Green synthesis and characterizations of bi-functional Mo-doped ZnO nanostructures for antimicrobial and photocatalytic applications, *Mater. Chem. Phys.*, 2023, **296**, 127306, DOI: **10.1016/j.matchemphys.2023.127306**.

13 S. S. Naik, S. J. Lee, S. Yeon, Y. Yu and M. Y. Choi, Pulsed laser-assisted synthesis of metal and nonmetal-co doped ZnO for efficient photocatalytic degradation of Rhodamine B under solar light irradiation, *Chemosphere*, 2021, **274**, 129782, DOI: **10.1016/j.chemosphere.2021.129782**.

14 A. Fiszka Borzyszkowska, A. Sulowska, I. Zekker, J. Karczewski, K. Bester and A. Zielińska-Jurek, Environmentally Friendly Fabrication of High-Efficient Fe-ZnO/Citric Acid-Modified Cellulose Composite and the Enhancement of Photocatalytic Activity in the Presence of H_2O_2, *Catalysts*, 2022, **12**, 1370, DOI: **10.3390/catal12111370**.

15 G. Xie, R. Jin, P. Ren, Y. Fang, R. Zhang and Z. Wang, Boosting CO_2 hydrogenation to methanol by adding trace amount of Au into Cu/ZnO catalysts, *Appl. Catal., B*, 2023, **324**, 122233, DOI: **10.1016/j.apcatb.2022.122233**.

16 Y.-C. Lin, C.-K. Peng, S.-C. Lim, C.-L. Chen, T.-N. Nguyen, T.-T. Wang, M.-C. Lin, Y.-J. Hsu, S.-Y. Chen and Y.-G. Lin, Tailoring the surface oxygen engineering of a carbon-quantum-dot-sensitized ZnO@H-ZnO_{1-x} multijunction toward efficient charge dynamics and photoactivity enhancement, *Appl. Catal., B*, 2021, **285**, 119846, DOI: **10.1016/j.apcatb.2020.119846**.

17 F. Zhao, X. Li, M. Zuo, Y. Liang, P. Qin, H. Wang, Z. Wu, L. Luo, C. Liu and L. Leng, Preparation of photocatalysts decorated by carbon quantum dots (CQDs) and their applications: a review, *J. Environ. Chem. Eng.*, 2023, **11**, 109487, DOI: **10.1016/j.jece.2023.109487**.

18 Z. Li, Q. Zhou, S. Li, M. Liu, Y. Li and C. Chen, Carbon dots fabricated by solid-phase carbonization using *p*-toluidine and l-cysteine for sensitive detection of copper, *Chemosphere*, 2022, **308**, 136298, DOI: **10.1016/j.chemosphere.2022.136298**.

19 Y. Hu, Y. Wang, C. Wang, Y. Ye, H. Zhao, J. Li, X. Lu, C. Mao, S. Chen, J. Mao, L. Wang and Q. Xue, One-pot pyrolysis preparation of carbon dots as eco-friendly nanoadditives of water-based lubricants, *Carbon*, 2019, **152**, 511–520, DOI: **10.1016/j.carbon.2019.06.047**.

20 F. Zhao, X. Li, T. Xiong, M. Zuo, L. Luo, P. Qin, M. Lei, Y. Liang, X. Gong, D. Zou and Z. Wu, Photocatalytic degradation of tetracycline by N-CQDs modified S-g-C_3N_4 nanotubes and its product toxicity evaluation, *Sep. Purif. Technol.*, 2023, **314**, 123533, DOI: **10.1016/j.seppur.2023.123533**.

21 F. Wen, P. Li, Y. Zhang, H. Zhong, H. Yan and W. Su, Preparation, characterization of green tea carbon quantum dots/curcumin antioxidant and antibacterial nanocomposites, *J. Mol. Struct.*, 2023, **1273**, 134247, DOI: **10.1016/j.molstruc.2022.134247**.

22 N. A. Qandeel, A. A. El-Masry, M. Eid, M. A. Moustafa and R. El-Shaheny, Fast one-pot microwave-assisted green synthesis of highly fluorescent plant-inspired S,N-self-doped carbon quantum dots as a sensitive probe for the antiviral drug nitazoxanide and hemoglobin, *Anal. Chim. Acta*, 2023, **1237**, 340592, DOI: **10.1016/j.aca.2022.340592**.

23 T. T. Vu Nu, N. H. Thi Tran, P. L. Truong, B. T. Phan, M. T. Nguyen Dinh, V.-P. Dinh, T. S. Phan, S. Go, M. Chang, K. T. Loan Trinh and V. Van Tran, Green synthesis of microalgae-based carbon dots for decoration of TiO_2 nanoparticles in enhancement of organic dye photodegradation, *Environ. Res.*, 2022, **206**, 112631, DOI: **10.1016/j.envres.2021.112631**.

24 D. Nagarajan, D. Gangadharan and S. Venkatanarasimhan, Synthetic strategies toward developing carbon dots via top-down approach, in *Carbon Dots in Analytical Chemistry*, Elsevier, 2023, pp. 1–13, DOI: **10.1016/B978-0-323-98350-1.00016-5**.

25 X. Li, F. Ge, X. Li, X. Zhou, J. Qian, G. Fu, L. Shi and Y. Xu, Rapid and large-scale production of carbon dots by salt-assisted electrochemical exfoliation of graphite rods, *J. Electroanal. Chem.*, 2019, **851**, 113390, DOI: **10.1016/j.jelechem.2019.113390**.

26 L. Cui, X. Ren, J. Wang and M. Sun, Synthesis of homogeneous carbon quantum dots by ultrafast dual-beam pulsed laser ablation for bioimaging, *Mater. Today Nano*, 2020, **12**, 100091, DOI: **10.1016/j.mtnano.2020.100091**.

27 Z.-A. Qiao, Y. Wang, Y. Gao, H. Li, T. Dai, Y. Liu and Q. Huo, Commercially activated carbon as the source for producing multicolor photoluminescent carbon dots by chemical oxidation, *Chem. Commun.*, 2010, **46**, 8812, DOI: **10.1039/c0cc02724c**.

28 V. Bressi, A. M. Balu, D. Iannazzo and C. Espro, Recent advances in the synthesis of carbon dots from renewable biomass by high-efficient hydrothermal and microwave green approaches, *Curr. Opin. Green Sustainable Chem.*, 2023, **40**, 100742, DOI: **10.1016/j.cogsc.2022.100742**.

29 V. Manikandan and N. Y. Lee, Green synthesis of carbon quantum dots and their environmental applications, *Environ. Res.*, 2022, **212**, 113283, DOI: **10.1016/j.envres.2022.113283**.

30 T. Yu, H. Wang, C. Guo, Y. Zhai, J. Yang and J. Yuan, A rapid microwave synthesis of green-emissive carbon dots with solid-state fluorescence and pH-sensitive properties, *R. Soc. Open Sci.*, 2018, **5**, 180245, DOI: **10.1098/rsos.180245**.

31 T. Arumugham, M. Alagumuthu, R. G. Amimodu, S. Munusamy and S. K. Iyer, A sustainable synthesis of green carbon quantum dot (CQD) from *Catharanthus roseus* (white flowering plant) leaves and investigation of its dual fluorescence responsive behavior in multi-ion detection and biological applications, *Sustainable Mater. Technol.*, 2020, **23**, e00138, DOI: 10.1016/j.susmat.2019.e00138.

32 I. Sargin, G. Yanalak, G. Arslan and I. H. Patir, Green synthesized carbon quantum dots as TiO_2 sensitizers for photocatalytic hydrogen evolution, *Int. J. Hydrogen Energy*, 2019, **44**, 21781–21789, DOI: 10.1016/j.ijhydene.2019.06.168.

33 J. Zhang, A. Xia, H. Chen, A.-S. Nizami, Y. Huang, X. Zhu, X. Zhu and Q. Liao, Biobased carbon dots production via hydrothermal conversion of microalgae Chlorella pyrenoidosa, *Sci. Total Environ.*, 2022, **839**, 156144, DOI: 10.1016/j.scitotenv.2022.156144.

34 C. Wang, L. Bi, J. Liu, B. Huang, F. Wang, Y. Zhang, C. Yao, G. Pan and M. Song, Microalgae-derived carbon quantum dots mediated formation of metal sulfide nano-adsorbents with exceptional cadmium removal performance, *J. Colloid Interface Sci.*, 2023, **629**, 994–1002, DOI: 10.1016/j.jcis.2022.08.188.

35 H. Widiyandari, O. Prilita, M. S. Al Ja'farawy, F. Nurosyid, O. Arutanti, Y. Astuti and N. Mufti, Nitrogen-doped carbon quantum dots supported zinc oxide (ZnO/N-CQD) nanoflower photocatalyst for methylene blue photodegradation, *Results Eng.*, 2023, **17**, 100814, DOI: 10.1016/j.rineng.2022.100814.

36 K. Akbar, E. Moretti and A. Vomiero, Carbon Dots for Photocatalytic Degradation of Aqueous Pollutants: Recent Advancements, *Adv. Opt. Mater.*, 2021, **9**, 2100532, DOI: 10.1002/adom.202100532.

37 V. Silva, J. F. A. Fernandes, M. C. Tomás, C. P. Silva, V. Calisto, M. Otero and D. L. D. Lima, Enhanced solar driven photocatalytic removal of antibiotics from aquaculture effluents by TiO_2/carbon quantum dot composites, *Catal. Today*, 2023, **419**, 114150, DOI: 10.1016/j.cattod.2023.114150.

38 H. Ren, F. Qi, A. Labidi, J. Zhao, H. Wang, Y. Xin, J. Luo and C. Wang, Chemically bonded carbon quantum dots/Bi_2WO_6 S-scheme heterojunction for boosted photocatalytic antibiotic degradation: interfacial engineering and mechanism insight, *Appl. Catal., B*, 2023, **330**, 122587, DOI: 10.1016/j.apcatb.2023.122587.

39 L. Xu, L. Yang, X. Bai, X. Du, Y. Wang and P. Jin, Persulfate activation towards organic decomposition and Cr(VI) reduction achieved by a novel CQDs-TiO_{2-x}/rGO nanocomposite, *Chem. Eng. J.*, 2019, **373**, 238–250, DOI: 10.1016/j.cej.2019.05.028.

40 M. Zhang, H. Tao, C. Zhai, J. Yang, Y. Zhou, D. Xia, G. Comodi and M. Zhu, Twin-brush ZnO mesocrystal for the piezo-activation of peroxymonosulfate to remove ibuprofen in water: performance and mechanism, *Appl. Catal., B*, 2023, **326**, 122399, DOI: 10.1016/j.apcatb.2023.122399.

41 J. Wang and S. Wang, Activation of persulfate (PS) and peroxymonosulfate (PMS) and application for the degradation of emerging contaminants, *Chem. Eng. J.*, 2018, **334**, 1502–1517, DOI: 10.1016/j.cej.2017.11.059.

42 M. Mahdi Ahmed, S. Barbati, P. Doumenq and S. Chiron, Sulfate radical anion oxidation of diclofenac and sulfamethoxazole for water decontamination, *Chem. Eng. J.*, 2012, **197**, 440–447, DOI: 10.1016/j.cej.2012.05.040.

43 S. Padhan, T. K. Rout and U. G. Nair, N-doped and Cu,N-doped carbon dots as corrosion inhibitor for mild steel corrosion in acid medium, *Colloids Surf., A*, 2022, **653**, 129905, DOI: 10.1016/j.colsurfa.2022.129905.

44 N. Vasimalai, V. Vilas-Boas, J. Gallo, M. de F. Cerqueira, M. Menéndez-Miranda, J. M. Costa-Fernández, L. Diéguez, B. Espiña and M. T. Fernández-Argüelles, Green synthesis of fluorescent carbon dots from spices for in vitro imaging and tumour cell growth inhibition, *Beilstein J. Nanotechnol.*, 2018, **9**, 530–544, DOI: 10.3762/bjnano.9.51.

45 S. Ren, M. Cui, X. Chen, S. Mei and Y. Qiang, Comparative study on corrosion inhibition of N doped and N,S co-doped carbon dots for carbon steel in strong acidic solution, *J. Colloid Interface Sci.*, 2022, **628**, 384–397, DOI: 10.1016/j.jcis.2022.08.070.

46 Z.-Q. Xu, L.-Y. Yang, X.-Y. Fan, J.-C. Jin, J. Mei, W. Peng, F.-L. Jiang, Q. Xiao and Y. Liu, Low temperature synthesis of highly stable phosphate functionalized two color carbon nanodots and their application in cell imaging, *Carbon*, 2014, **66**, 351–360, DOI: 10.1016/j.carbon.2013.09.010.

47 I. M. Weiss, C. Muth, R. Drumm and H. O. K. Kirchner, Thermal decomposition of the amino acids glycine, cysteine, aspartic acid, asparagine, glutamic acid, glutamine, arginine and histidine, *BMC Biophys.*, 2018, **11**, 2, DOI: 10.1186/s13628-018-0042-4.

48 M. Koinuma, H. Tateishi, K. Hatakeyama, S. Miyamoto, C. Ogata, A. Funatsu, T. Taniguchi and Y. Matsumoto, Analysis of Reduced Graphene Oxides by X-ray Photoelectron Spectroscopy and Electrochemical Capacitance, *Chem. Lett.*, 2013, **42**, 924–926, DOI: 10.1246/cl.130152.

49 G. Radaelli, J. A. Heredia-Guerrero, M. T. Masood, L. Ceseracciu, A. Davis, R. Carzino, M. Prato, I. S. Bayer and A. Athanassiou, Highly Effective Antiadhesive Coatings from pH-Modified Water-Dispersed Perfluorinated Acrylic Copolymers: The Case of Vulcanizing Rubber, *Adv. Mater. Interfaces*, 2016, **3**, 1600069, DOI: 10.1002/admi.201600069.

50 M. K. Rabchinskii, S. A. Ryzhkov, D. A. Kirilenko, N. V. Ulin, M. V. Baidakova, V. V. Shnitov, S. I. Pavlov, R. G. Chumakov, D. Y. Stolyarova, N. A. Besedina, A. V. Shvidchenko, D. V. Potorochin, F. Roth, D. A. Smirnov, M. V. Gudkov, M. Brzhezinskaya, O. I. Lebedev, V. P. Melnikov and P. N. Brunkov, From graphene oxide towards aminated graphene: facile synthesis, its structure and electronic properties, *Sci. Rep.*, 2020, **10**, 6902, DOI: 10.1038/s41598-020-63935-3.

51 N. Calisi, S. Martinuzzi, A. Giaccherini, C. S. Pomelli, L. Guazzelli and S. Caporali, Temperature and angle resolved XPS study of BMIm Cl and BMIm $FeCl_4$, *J.

Electron Spectrosc. Relat. Phenom., 2021, **247**, 147034, DOI: **10.1016/j.elspec.2020.147034**.

52 M. Wagstaffe, A. G. Thomas, M. J. Jackman, M. Torres-Molina, K. L. Syres and K. Handrup, An Experimental Investigation of the Adsorption of a Phosphonic Acid on the Anatase TiO_2 (101) Surface, *J. Phys. Chem. C*, 2016, **120**, 1693–1700, DOI: **10.1021/acs.jpcc.5b11258**.

53 N. Tawil, E. Sacher, E. Boulais, R. Mandeville and M. Meunier, X-ray Photoelectron Spectroscopic and Transmission Electron Microscopic Characterizations of Bacteriophage–Nanoparticle Complexes for Pathogen Detection, *J. Phys. Chem. C*, 2013, **117**, 20656–20665, DOI: **10.1021/jp406148h**.

54 R. Arrigo, M. Hävecker, S. Wrabetz, R. Blume, M. Lerch, J. McGregor, E. P. J. Parrott, J. A. Zeitler, L. F. Gladden, A. Knop-Gericke, R. Schlögl and D. S. Su, Tuning the Acid/Base Properties of Nanocarbons by Functionalization via Amination, *J. Am. Chem. Soc.*, 2010, **132**, 9616–9630, DOI: **10.1021/ja910169v**.

55 M. Raicopol, C. Andronescu, R. Atasiei, A. Hanganu and L. Pilan, Post-Polymerization Electrochemical Functionalization of a Conducting Polymer: Diazonium Salt Electroreduction at Polypyrrole Electrodes, *J. Electrochem. Soc.*, 2014, **161**, G103–G113, DOI: **10.1149/2.0871412jes**.

56 K. Jlassi, K. Eid, M. H. Sliem, A. M. Abdullah, M. M. Chehimi and I. Krupa, Rational synthesis, characterization, and application of environmentally friendly (polymer–carbon dot) hybrid composite film for fast and efficient UV-assisted Cd^{2+} removal from water, *Environ. Sci. Eur.*, 2020, **32**, 12, DOI: **10.1186/s12302-020-0292-z**.

57 N. R. Devi, T. H. V. Kumar and A. K. Sundramoorthy, Electrochemically Exfoliated Carbon Quantum Dots Modified Electrodes for Detection of Dopamine Neurotransmitter, *J. Electrochem. Soc.*, 2018, **165**, G3112–G3119, DOI: **10.1149/2.0191812jes**.

58 D. Gu, L. Hong, L. Zhang, H. Liu and S. Shang, Nitrogen and sulfur co-doped highly luminescent carbon dots for sensitive detection of Cd(II) ions and living cell imaging applications, *J. Photochem. Photobiol., B*, 2018, **186**, 144–151, DOI: **10.1016/j.jphotobiol.2018.07.012**.

59 K. Jiang, S. Sun, L. Zhang, Y. Lu, A. Wu, C. Cai and H. Lin, Red, Green, and Blue Luminescence by Carbon Dots: Full-Color Emission Tuning and Multicolor Cellular Imaging, *Angew. Chem., Int. Ed.*, 2015, **54**, 5360–5363, DOI: **10.1002/anie.201501193**.

60 S. S. Mohtar, F. Aziz, A. F. Ismail, N. S. Sambudi, H. Abdullah, A. N. Rosli and B. Ohtani, Impact of Doping and Additive Applications on Photocatalyst Textural Properties in Removing Organic Pollutants: A Review, *Catalysts*, 2021, **11**, 1160, DOI: **10.3390/catal11101160**.

61 S. Muthulingam, K. B. Bae, R. Khan, I.-H. Lee and P. Uthirakumar, Improved daylight-induced photocatalytic performance and suppressed photocorrosion of N-doped ZnO decorated with carbon quantum dots, *RSC Adv.*, 2015, **5**, 46247–46251, DOI: **10.1039/C5RA07811C**.

62 S. Song, K. Wu, H. Wu, J. Guo and L. Zhang, Multi-shelled ZnO decorated with nitrogen and phosphorus co-doped carbon quantum dots: synthesis and enhanced photodegradation activity of methylene blue in aqueous solutions, *RSC Adv.*, 2019, **9**, 7362–7374, DOI: **10.1039/C9RA00168A**.

63 M. S. Nadeem, T. Munawar, F. Mukhtar, M. Naveed ur Rahman, M. Riaz and F. Iqbal, Enhancement in the photocatalytic and antimicrobial properties of ZnO nanoparticles by structural variations and energy bandgap tuning through Fe and Co co-doping, *Ceram. Int.*, 2021, **47**, 11109–11121, DOI: **10.1016/j.ceramint.2020.12.234**.

64 D. Neena, M. Humayun, W. Zuo, C. S. Liu, W. Gao and D. J. Fu, Hierarchical hetero-architectures of in situ g-C_3N_4-coupled Fe-doped ZnO micro-flowers with enhanced visible-light photocatalytic activities, *Appl. Surf. Sci.*, 2020, **506**, 145017, DOI: **10.1016/j.apsusc.2019.145017**.

65 S. M. Yakout and A. M. El-Sayed, Enhanced ferromagnetic and photocatalytic properties in Mn or Fe doped p-CuO/n-ZnO nanocomposites, *Adv. Powder Technol.*, 2019, **30**, 2841–2850, DOI: **10.1016/j.apt.2019.08.033**.

66 A. Raza, M. Shoeb, F. Mashkoor, S. Rahaman, M. Mobin, C. Jeong, M. Yusuf Ansari and A. Ahmad, Phoenix dactylifera mediated green synthesis of Mn doped ZnO nanoparticles and its adsorption performance for methyl orange dye removal: a comparative study, *Mater. Chem. Phys.*, 2022, **286**, 126173, DOI: **10.1016/j.matchemphys.2022.126173**.

67 D. K. Singh, D. K. Pandey, R. R. Yadav and D. Singh, A study of nanosized zinc oxide and its nanofluid, *Pramana*, 2012, **78**, 759–766, DOI: **10.1007/s12043-012-0275-8**.

68 K. Xiong, K. Wang, L. Chen, X. Wang, Q. Fan, J. Courtois, Y. Liu, X. Tuo and M. Yan, Heterostructured $ZnFe_2O_4$/Fe_2TiO_5/TiO_2 Composite Nanotube Arrays with an Improved Photocatalysis Degradation Efficiency Under Simulated Sunlight Irradiation, *Nano-Micro Lett.*, 2018, **10**, 17, DOI: **10.1007/s40820-017-0169-x**.

69 K. H. Praveen and A. S. Prasad, Chrysin mediated synthesis, crystallographic structure and optical emission characteristics of ZnO nanoparticles, *Mater. Today: Proc.*, 2021, **41**, 590–595, DOI: **10.1016/j.matpr.2020.05.254**.

70 R. Khokhra, B. Bharti, H.-N. Lee and R. Kumar, Visible and UV photo-detection in ZnO nanostructured thin films via simple tuning of solution method, *Sci. Rep.*, 2017, **7**, 15032, DOI: **10.1038/s41598-017-15125-x**.

71 A. Anjum, R. Ahmed, Z. A. Umar, S. Azzam, T. Hussain, M. N. Sarwar and M. A. Baig, Structure and defects-related optical properties of highly (002)-oriented zinc oxide thin films, *Phys. B*, 2022, **644**, 414195, DOI: **10.1016/j.physb.2022.414195**.

72 L. Al-Farsi, T. M. Souier, M. Al-Hinai, M. T. Z. Myint, H. H. Kyaw, H. M. Widatallah and M. Al-Abri, pH Controlled Nanostructure and Optical Properties of ZnO and Al-Doped ZnO Nanorod Arrays Grown by Microwave-Assisted Hydrothermal Method, *Nanomaterials*, 2022, **12**, 3735, DOI: **10.3390/nano12213735**.

73 A. Galdámez-Martinez, G. Santana, F. Güell, P. R. Martínez-Alanis and A. Dutt, Photoluminescence of ZnO Nanowires: A Review, *Nanomaterials*, 2020, **10**, 857, DOI: **10.3390/nano10050857**.

74 V. Kumar, H. C. Swart, O. M. Ntwaeaborwa, R. E. Kroon, J. J. Terblans, S. K. K. Shaat, A. Yousif and M. M. Duvenhage, Origin of the red emission in zinc oxide nanophosphors, *Mater. Lett.*, 2013, **101**, 57–60, DOI: **10.1016/j.matlet.2013.03.073**.

75 W. Jia, S. Dang, H. Liu, Z. Zhang, C. Yu, X. Liu and B. Xu, Evidence of the formation mechanism of ZnO in aqueous solution, *Mater. Lett.*, 2012, **82**, 99–101, DOI: **10.1016/j.matlet.2012.05.013**.

76 F. V. Molefe, L. F. Koao, B. F. Dejene and H. C. Swart, Phase formation of hexagonal wurtzite ZnO through decomposition of $Zn(OH)_2$ at various growth temperatures using CBD method, *Opt. Mater.*, 2015, **46**, 292–298, DOI: **10.1016/j.optmat.2015.04.034**.

77 H. Fang, Y. Gao, G. Li, J. An, P.-K. Wong, H. Fu, S. Yao, X. Nie and T. An, Advanced Oxidation Kinetics and Mechanism of Preservative Propylparaben Degradation in Aqueous Suspension of TiO_2 and Risk Assessment of Its Degradation Products, *Environ. Sci. Technol.*, 2013, **47**, 2704–2712, DOI: **10.1021/es304898r**.

78 Y. Song, J. Tian, S. Gao, P. Shao, J. Qi and F. Cui, Photodegradation of sulfonamides by g-C_3N_4 under visible light irradiation: effectiveness, mechanism and pathways, *Appl. Catal., B*, 2017, **210**, 88–96, DOI: **10.1016/j.apcatb.2017.03.059**.

79 Y. Liu, Y. Zhang, H. Guo, X. Cheng, H. Liu and W. Tang, Persulfate-assisted photodegradation of diethylstilbestrol using monoclinic $BiVO_4$ under visible-light irradiation, *Environ. Sci. Pollut. Res.*, 2017, **24**, 3739–3747, DOI: **10.1007/s11356-016-8020-3**.

80 Y. Gao, Z. Chen, Y. Zhu, T. Li and C. Hu, New Insights into the Generation of Singlet Oxygen in the Metal-Free Peroxymonosulfate Activation Process: Important Role of Electron-Deficient Carbon Atoms, *Environ. Sci. Technol.*, 2020, **54**, 1232–1241, DOI: **10.1021/acs.est.9b05856**.

81 J. Yu, H. Feng, L. Tang, Y. Pang, G. Zeng, Y. Lu, H. Dong, J. Wang, Y. Liu, C. Feng, J. Wang, B. Peng and S. Ye, Metal-free carbon materials for persulfate-based advanced oxidation process: microstructure, property and tailoring, *Prog. Mater. Sci.*, 2020, **111**, 100654, DOI: **10.1016/j.pmatsci.2020.100654**.

82 Y. Gao, T. Li, Y. Zhu, Z. Chen, J. Liang, Q. Zeng, L. Lyu and C. Hu, Highly nitrogen-doped porous carbon transformed from graphitic carbon nitride for efficient metal-free catalysis, *J. Hazard. Mater.*, 2020, **393**, 121280, DOI: **10.1016/j.jhazmat.2019.121280**.

83 Y. Jiang, Z. Wang, J. Huang, F. Yan, Y. Du, C. He, Y. Liu, G. Yao and B. Lai, A singlet oxygen dominated process through photocatalysis of CuS-modified MIL-101(Fe) assisted by peroxymonosulfate for efficient water disinfection, *Chem. Eng. J.*, 2022, **439**, 135788, DOI: **10.1016/j.cej.2022.135788**.

84 T. H. Nghia, V. T. Khanh, C. T. Vu, N. T. K. Oanh, N. T. Van Anh, L. H. Luyen, N. Negishi, S. Ouillon and B. Van Hoi, Removal of Carbamazepine in Aqueous Solution by TiO_2 Ceramic Photo-Catalyst under Simulated Solar Light: Kinetics, Effects of Environmental Factors and Degradation Pathways, *Water*, 2023, **15**, 1583, DOI: **10.3390/w15081583**.

85 D. G. Ayu, S. Gea, A. Andriayani, D. J. Telaumbanua, A. F. R. Piliang, M. Harahap, Z. Yen, R. Goei and A. I. Y. Tok, Photocatalytic Degradation of Methylene Blue Using N-Doped ZnO/Carbon Dot (N-ZnO/CD) Nanocomposites Derived from Organic Soybean, *ACS Omega*, 2023, **8**, 14965–14984, DOI: **10.1021/acsomega.2c07546**.

86 X. Gao, X. Liu, Z. Zhu, X. Wang and Z. Xie, Enhanced photoelectrochemical and photocatalytic behaviors of MFe_2O_4 (M = Ni, Co, Zn and Sr) modified TiO_2 nanorod arrays, *Sci. Rep.*, 2016, **6**, 30543, DOI: **10.1038/srep30543**.

87 Y. Nosaka and A. Y. Nosaka, Generation and Detection of Reactive Oxygen Species in Photocatalysis, *Chem. Rev.*, 2017, **117**, 11302–11336, DOI: **10.1021/acs.chemrev.7b00161**.